

**COLLECTIVE RESPONSE OF
NETWORKS OF COLPITTS OSCILLATORS COUPLED UNIDIRECTIONALLY**

A Thesis
Presented to the
Faculty of
San Diego State University

In Partial Fulfillment
of the Requirements for the Degree
Master of Science in Applied Mathematics
with a Concentration in
Dynamical Systems

by
Horacio Lopez
Summer 2019

SAN DIEGO STATE UNIVERSITY

The Undersigned Faculty Committee Approves the

Thesis of Horacio Lopez:

Collective Response of

Networks of Colpitts Oscillators Coupled Unidirectionally

Antonio Palacios, Chair
Department of Mathematics and Statistics

Peter Blomgren
Department of Mathematics and Statistics

Luciano Demasi
Department of Aerospace Engineering

Approval Date

Copyright © 2019
by
Horacio Lopez.

DEDICATION

To all my loved ones for their unconditional support.

Mathematics is, I believe, the chief source of the belief in eternal and exact truth, as well as a super-sensible intelligible world.

– Bertrand Russell

ABSTRACT OF THE THESIS

Collective Response of
Networks of Colpitts Oscillators Coupled Unidirectionally
by
Horacio Lopez

Master of Science in Applied Mathematics with a Concentration in Dynamical Systems
San Diego State University, 2019

Highly accurate precision timing devices are crucial to our modern world. Financial, electric, navigation, and many other systems rely heavily on accurate time measurements for synchronization. Currently, most applications and systems that depend on precision timing work off of the Global Positioning System's signal.

This thesis presents a nonlinear analysis performed on the a of equations that serve as a model for networks of unidirectional coupled Colpitts oscillators. The motivation for these networks lies on their potential to reduce phase drift error through collective behavior. We strive to create an ultra-precision timing system from N numbered Coupled Colpitts Oscillators. This timing device would work independent of the Global Positioning System network and offer robust, accurate timing in environments where devices that rely on the satellite network might fail. We investigate the collective patterns of oscillations that can arise via symmetry breaking bifurcations. By analyzing the symmetry and stability properties of the highly nonlinear governing equations to find phase shift synchronization, we take advantage of the scaling error decrease to achieve better precision timing.

TABLE OF CONTENTS

	PAGE
ABSTRACT	vi
LIST OF TABLES.....	viii
LIST OF FIGURES	ix
ACKNOWLEDGMENTS	xv
CHAPTER	
1 INTRODUCTION	1
2 Nonlinear Oscillators	4
2.1 Duffing Oscillator	5
2.2 Van der Pol Oscillator.....	7
2.3 Crystal Oscillators.....	9
2.4 Colpitts Oscillator: Circuit Model.....	11
2.5 Colpitts Oscillator: Ideal Model	14
3 Network of Unidirectionally Coupled Colpitts Oscillators: Circuit Model	20
3.1 Governing Equations.....	20
3.2 Consequences of Symmetry	21
3.3 Computational Bifurcation Analysis	27
3.4 Basins of Attraction	36
3.5 Phase-Drift Calculations	41
4 Network with Ideal Model.....	45
4.1 Governing Equations.....	45
4.2 Asymptotic Approximation of Eigenvalues.....	45
4.3 Computational Bifurcation Analysis	49
5 Experiments	58
6 Discussion and Future Work.....	61
BIBLIOGRAPHY	62

LIST OF TABLES

	PAGE
2.1 Colpitts Oscillator Circuit Parameters	13
3.1 Symmetry Groups: N=3	24
3.2 Symmetry Groups: N=4	25
3.3 Symmetry Groups: N=5	26
3.4 Symmetry Groups: N=6	27

LIST OF FIGURES

	PAGE
1.1 Picture of NIST-F1 cesium fountain atomic clock. The uncertainty was measured at a 3×10^{-16} as of January 2013. Source: M. A. WEISS, <i>F1 cesium fountain atomic clock</i> , Oct 2018.	2
2.1 Energy potential for Duffing oscillator without forcing. As we can see, when we remove the damping parameter, $\delta = 0$, we have Hamiltonian system. The system has single-well potential for parameter $\beta > 0$ and a double-well potential for $\beta < 0$. Source: T. KANAMARU, <i>Duffing oscillator</i> , Scholarpedia, 3 (2008), p.6327. revision #91210.	5
2.2 Undamped case (a) and damped case (b) for $\beta < 1$ with the single-well potential plot. Undamped case (c) and damped case (d) for $\beta > 1$ with the double-well potential plot. Panel (d) shows that the damped case converges to two different stable equilibria.	6
2.3 Circuit for the Van der Pol oscillator where its current-voltage characteristic, $V = f(I)$, resembles a cubic function. Source: S. STROGATZ, <i>Nonlinear Dynamics and Chaos: With Applications to Physics, Biology, Chemistry, and Engineering</i> , Studies in Nonlinearity, Avalon Publishing, 2014.	7
2.4 Phase plane of the Van der Pol oscillator with the variable transformation seen above and $\epsilon = 5$. We can see that it follows the trajectory of the cubic nullcline, $F(x)$, and quickly jumps horizontally once it reaches either of the local minima/maxima. These type of oscillations where we have a slow buildup followed by a quick discharge are called “relaxation oscillations.”	8
2.5 Solution of the Van der Pol system vs time. The characteristic “relaxation oscillations” can also be seen in this plot.	8
2.6 Circuit diagram for quartz crystal oscillators. This is a two-mode crystal oscillator circuit. A second set of RLC components are introduced by parasitic elements. Source: P. BUONO, B. CHAN, J. FERREIRA, A. PALACIOS, S. REEVES, P. LONGHINI, AND V. IN, <i>Symmetry-breaking bifurcations and patterns of oscillations in rings of crystal oscillators</i> , SIAM Journal on Applied Dynamical Systems, 17 (2018), pp. 1310-1352.	9

2.7	Experimental measurements for N=2 and N=3 oscillators revealing the predicted traveling wave pattern. Source: P. BUONO, B. CHAN, J. FERREIRA, A. PALACIOS, S. REEVES, P. LONGHINI, AND V. IN, <i>Symmetry-breaking bifurcations and patterns of oscillations in rings of crystal oscillators</i> , SIAM Journal on Applied Dynamical Systems, 17 (2018), pp. 1310-1352.	10
2.8	Log scaled phase error vs N for RW1 type solutions: Traveling Wave also known as phase drift by T/N solutions; RW2 solutions: phase drift by $T/2$ solutions; and Synchronized, fully in phase solutions. A least squared regression line is fit to data for each different solution type. Source: P. BUONO, B. CHAN, J. FERREIRA, A. PALACIOS, S. REEVES, P. LONGHINI, AND V. IN, <i>Symmetry-breaking bifurcations and patterns of oscillations in rings of crystal oscillators</i> , SIAM Journal on Applied Dynamical Systems, 17 (2018), pp. 1310-1352.	11
2.9	Single Colpitts Circuit Diagram	12
2.10	Solution of the system vs time of all three system components of circuit equations.	13
2.11	Solution phase plane for all three system components.	14
2.12	Solution of the ideal model system vs time. $g = 1.1$, $Q = 1$, and $\kappa = .5$. Note the difference in time scaling and simplification of oscillations when compared to the circuit model.	15
2.13	One-parameter bifurcation diagram of a reduced model for a Colpitts oscillator. Solid lines represent stable equilibria, dashed lines represent unstable equilibria, filled-in circles represent stable orbits, and empty circles represent unstable orbits. We see the emergence of stable limit cycles at the Hopf bifurcation at $g = 1$. These stable limit cycles remain quasi-sinusoidal until the emergence of period doubling at approximately $g = 4$. A cascade of period doubling not detailed in the plot emerges in the vicinity of the first period doubling bifurcation. This period doubling behavior reverts and re-emerges as g increases and moves away from the Hopf bifurcation.	18

2.14	Two-parameter bifurcation diagram of a reduced model for a Colpitts Oscillator. A Hopf locus persist at $g = 1$ for all values of Q . The Hopf locus is traced by a vertical, solid line. For values of $Q < 0$ a Hopf bifurcation at $g = 1$ leads to unstable limit cycles. The physically relevant case, $Q > 0$, has a Hopf bifurcation at $g = 1$, which produces stable limit cycles. These two cases are seen in the subfigures plotting the norm of the system, $\ X\ $, vs values of g . Dashed lines represent unstable equilibrium points; solid lines represent stable equilibria; empty circles denote unstable limit cycles; closed circles represent stable limit cycles. The stable limit cycles become more sinusoidal as g is chosen near the Hopf point. This can be seen in the subfigures showing the time solution of the first component vs time.	19
3.1	Concept diagram for network of N coupled oscillators	20
3.2	Network of six oscillators coupled unidirectionally. Same colored nodes represent in phase oscillations. Every oscillator is labeled with its respective phase shift generated by $\gamma^3 = \langle \frac{T}{2} \rangle$ where T is the oscillator's period.	24
3.3	IP behavior for $N = 3$ for (3.1). Solution for voltage component, V_C , of three CCO with coupling strength $\lambda = 0.1$ (a). We can see a complete overlap of solutions between the three oscillators which indicates perfect IP behavior. Phase diagram of V_C solutions for all three CCOs with coupling strength value $\lambda = 0.1$ (b). The straight line shows complete IP synchronization between the three oscillators.	25
3.4	TW behavior for NCCOs with three oscillators. Solution for V_C component vs time for three CCOs at $\lambda = -0.1$. We can see the phase shift synchronization between oscillator.	25
3.5	Network of four oscillators coupled unidirectionally. Same colored nodes represent in phase oscillations. Every oscillator is labeled with its respective phase shift generated by $\gamma^2 = \langle \frac{T}{2} \rangle$ where T is the oscillator's period.	26
3.6	Network of six oscillators coupled unidirectionally. Same colored nodes represent in phase oscillations. Every oscillator is labeled with its respective phase shift generated by $\gamma^2 = \langle \frac{T}{3} \rangle$ where T is the oscillator's period.	27
3.7	Here we see the bifurcation diagram for the governing equations of a Network with three unidirectionally coupled Colpitts oscillators. made using AUTO and MATLAB. We plot the norm of the system vs the coupling strength parameter λ	28

3.8	Two-parameter bifurcation performed on the system with resistance vs coupling strength axis. The lines represent Hopf bifurcation locus. Both type of TW solutions can be seen on the left side of the Hopf bifurcation locus. Their solution stability depends on the coupling strength value and initial conditions.	30
3.9	Bifurcation diagram for the case of four coupled Colpitts oscillators plotted in norm vs coupling strength axis.	30
3.10	This is a magnification of Fig. 3.9 for $0 < \ X\ < 8.5$ where HB_1 branches off into unstable SW type orbits. Note the complexity and abundance of limit points.	31
3.11	Two-parameter bifurcation diagram of resistance vs coupling strength. The lines represent Hopf bifurcation locus. As with the previous case, TW and SW type solutions exist to the left of the Hopf bifurcation locus, and the stability of such orbits depend on initial conditions and coupling strength.	32
3.12	Bifurcation diagram shown in norm of system vs coupling strength plot for a NCCOs composed of five oscillators. All four Hopf bifurcations led to their unique set of stable TW orbits with different behavior.	33
3.13	Two-parameter bifurcation diagram of resistance vs coupling strength for $N = 5$ oscillators. The lines represent Hopf Bifurcations. These traveling wave solutions exist only to the left side of their respective Hopf locus. Stability of these TW depend on initial conditions and coupling strength.	34
3.14	This is the bifurcation diagram for the case $N = 6$ plotted in a norm vs coupling strength axis. Three of the five Hopf bifurcations lead to large branches of stable and unstable orbits, but HB_2 has a shorter branch that AUTO was not able to expand. We show only the branches that AUTO produced.	35
3.15	Fig. (3.14) expanded about Hopf bifurcations HB_1 to HB_4 . The stable SW can be seen close to $\lambda = 0$	35
3.16	Two-parameter bifurcation diagram of R_L vs λ . The lines represent Hopf bifurcation locus. The stability of the orbits depend on initial condition and coupling strength.	36
3.17	Probability distribution of solution types for different coupling strength values for the case of three coupled Colpitts oscillators.	38
3.18	Probability density for different solution types of the case of four coupled Colpitts oscillators. We can see that the negative regime of the plot displays richer dynamics than that of case $N = 3$	39
3.19	Probability density for different solution types for the case of five CCOs. The behavior seen here is similar to the case $N = 3$	40

3.20	Probability density plot for different solution types of the case with six coupled Colpitts oscillators. In this scenario, we do not differentiate between the two different type of SW solutions. Instead, we classify them both as SW. It is apparent that the dynamics become more complex, and numerical classification becomes more difficult due to the higher number of oscillators and increase in the transient time needed to fully converge to a solution.	40
3.21	Voltage portion of the solution for the circuit model in Langevin form. The bottom plot, η , shows the colored noise obtained through the Ornstein-Uhlenbeck process. Note the difference in magnitudes between the noise and the actual solution of the system.	42
3.22	Phase drift error calculations for uncoupled oscillators. The phase drift was calculated for 20 samples and averaged for each case of number of oscillators. A least square linear regression line is plotted on the Log of the phase drift vs the Log of the number of oscillators, N . The slope, m , represents the scaling exponent, $1/N^m$. This validates the prediction that uncoupled oscillators have a phase error scaling of $1/\sqrt{N}$	43
3.23	Tentative results for phase drift calculations with noise level $D = 1 \times 10^{-13}$ chosen through experimentation. The values of the y-axis display the scaling exponent m which corresponds to scaling $1/N^m$. Iterations through small, negative λ values yielded a small region where we see scaling improvement approaching $1/N$	43
4.1	One-parameter bifurcation diagram as a function of λ for the ideal model with $N = 3$. Note that the stable orbit regions are qualitatively similar to those in the circuit model bifurcation diagram.	50
4.2	Two-parameter bifurcation diagram showing the Hopf bifurcation locus. Note that for large enough fixed values of g , the locus corresponding to HB_1 will cross the fixed g space twice.	51
4.3	(a) One-parameter bifurcation diagram of varying λ for the ideal model representing the case of four coupled Colpitts Oscillators. (b) Close up to trivial solution and Hopf bifurcations.	52
4.4	Two-parameter bifurcation diagram varying λ and R_L for the ideal model representing the case of four coupled oscillators.	53
4.5	One-parameter bifurcation diagram of varying λ for the system describing the ideal model of five coupled Colpitts oscillators.	54
4.6	Two-parameter bifurcation diagram for the system describing the ideal model of five coupled Colpitts oscillators.	54
4.7	(a) One-parameter bifurcation diagram of varying λ for the ideal model of six coupled Colpitts oscillators. (b) Close up to trivial solution and Hopf bifurcations.	56

4.8	Two-parameter bifurcation diagram of the ideal model with six coupled Colpitts oscillators.	57
5.1	PCB prototype with nine unidirectionally coupled oscillators. It allows for controlling the number of active Colpitts oscillators.	58
5.2	Measured phase drift improvement for ensembles of five and seven oscillators. The improvement approaches the desired $1/N$ scaling.	59
5.3	PCB design for voltage measurement of chip-scale NCCO.	59
5.4	Measured sum output of three chip-scale colpitts oscillators.	60

ACKNOWLEDGMENTS

I would like to thank all of my undergraduate and graduate professors at San Diego State University who introduced me to the wonderful world of Applied Math. I would especially like to thank my adviser Dr. Antonio Palacios for all of his help and patience. His expertise and passion for mathematics kept me motivated throughout my studies.

I would also like to thank the Office of Naval Research (ONR), the NREIP summer internship, and Dr. Patrick Longhini and Dr. Visarath In at NWIC Pacific for their support. It was a pleasure working with the team at NWIC. The experience left me with invaluable knowledge.

This thesis would not have been possible without the help and support of my friends at SDSU. The moral support and encouragement I received from all of you these past two years was invaluable.

CHAPTER 1

INTRODUCTION

Highly accurate precision timing devices are crucial to our modern world. Financial, electric, navigation, and many other systems rely heavily on accurate time measurements for synchronization. The need for accurate time keeping is always increasing. Most applications and systems that depend on precision timing employ the Global Positioning System's (GPS) signal. GPS relays time from a network of atomic clocks orbiting Earth in satellites. This ultra precise time measurement is accessible from almost anywhere on Earth.

In this thesis we set up the framework to build an ultra precision timing device that could provide an alternative for use in areas where GPS is not readily accessible. The device consists of Networks of Coupled Colpitts Oscillators (NCCOs). Through mathematical analysis of the system, engineering, and physics, we aim to minimize the time error of the ensemble. The concept behind the device lies in the mathematics and dynamics of networks of nonlinear oscillators such as the crystal quartz oscillator and the Colpitts oscillator. All timing devices exhibit timing error in the form of phase drift. A common practice to improve measurements of time is to gather the output of a collection of timing devices, such as N atomic clocks, and average out the time readings from all clocks. Logically and in practice, this leads to a more accurate time measurement. The decrease in the phase error follows the scaling $1/\sqrt{N}$.

We seek to improve this scaling to $1/N$. This is done by having a network of coupled Colpitts oscillators (NCCOs) operate in a traveling wave solution. A traveling wave solution is when all components oscillate at the same frequency but are out of phase from each other by T/N where T is the oscillation period. Such solutions have the ability to reduce phase drift error thus improving the measurement of time.

The oldest timing devices implemented by mankind are circulating the cosmos right now. Civilization has used the stars and moon as tools to measure the passing of months and years. On a smaller time scale, the passing of the sun has been used as a way to measure the passage of days. Humanity eventually started creating devices to keep up with the needs of society. Early Egyptians used solar clocks as a way to partition the length of a day into smaller units of measurement. The disadvantage of such a device was that it had to be re-calibrated according to the position of the sun and was useless at night or on cloudy days [3]. Eastern civilizations used the candle clock which consisted of marking a candle at regular intervals and lighting it [3]. When the flame would melt a candle down, the markings were

used as a unit of time. Not only were they dangerous, but a breeze or a light rain would render them useless outdoors. Better devices were invented as centuries passed, but creating accurate and useful timing mechanisms that worked on a boat navigating the open seas remained a challenge, as accurately determining longitude requires highly precise timing. This problem remained unsolved until the invention of the ship's chronometer in the early 18th century [3]. This technology remained in use until the development of electronic oscillators, which revolutionized many areas of industry from timing devices to radio equipment [16]. Variations of these oscillators remained the norm until the creation of the first atomic clock in 1948. This device worked by measuring the spectroscopic absorption line of ammonia, but was less portable and accurate than the quartz oscillator clock [15]. It was soon updated to a cesium atomic beam device. In 1973, GPS was launched by the U.S. AirForce. Satellites carrying space-qualified atomic clocks were sent to orbit Earth with the purpose of recording 3-dimensional position data and 1-dimensional time data.

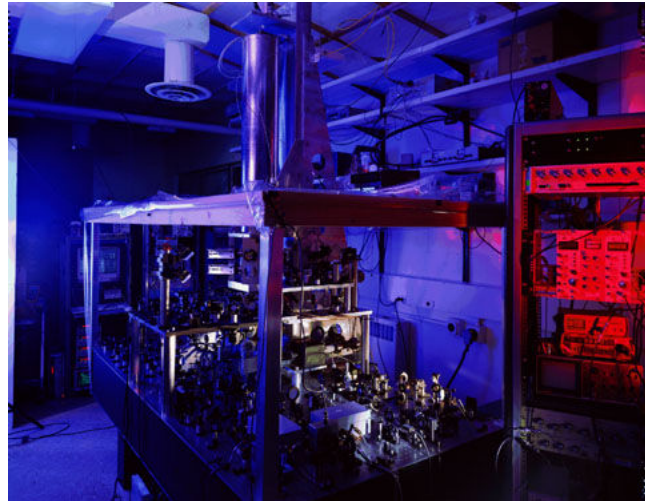


Figure 1.1. Picture of NIST-F1 cesium fountain atomic clock. The uncertainty was measured at a 3×10^{-16} as of January 2013. Source: M. A. WEISS, *F1 cesium fountain atomic clock*, Oct 2018.

Typical atomic clocks cost around \$40,000 and are not built to be portable. A picture of the NIST-F1 cesium fountain atomic clock can be seen in Fig. 1.1. The NIST-F2 clock which is accurate to the order of 1×10^{-16} requires being shielded in a cold environment making portability an even bigger issue [2]. Since atomic clocks themselves are logically difficult to carry around, most technologies depend on GPS. However, GPS signal can be lost in certain types of terrains, and thus, is not useful in all environments. The timing device composed of NCCOs offers a solution to manufacturing cost and portability issues.

This thesis is organized as follows. Chapter 2 lays out the background and mathematical analysis of the Colpitts oscillator. Chapter 3 includes a description of the NCCO circuit model with unidirectional coupling along with the mathematical analysis of its governing equation. The analysis includes a classification of all possible solutions that arise as a consequence of the system's (\mathbb{Z}_N, S^1) symmetry, numerical bifurcation analysis, approximations of the basins of attraction of different patterns, and phase drift calculations. In Chapter 4, we analyze a reduced, normalized form of the circuit model, the Ideal Model. We introduce the reduced equations, and by reducing the system's dimensionality via an isotypic decomposition of the phase space, we approximate the system's eigenvalues. In Chapter 5, the experiments performed on actual prototypes of the timing device are described. Finally, Chapter 6 contains the conclusion with a discussion of the work outlined in this thesis and future work.

CHAPTER 2

NONLINEAR OSCILLATORS

Time keeping devices require a way to “keep a beat” as precisely as possible. In other words, they need some type of oscillatory mechanism that allows it to keep time. The higher the precision of the oscillator, the higher precision time can be kept. In mathematics, oscillators with exact period and frequency exist in abundance, but the oscillators found or built in the real world are not perfect. If we are to model these real world oscillators to high precision, we must include the nonlinearities that these complicated systems exhibit. However, analysis of nonlinear oscillators is not always a trivial matter.

Mathematically, a system modeling a linear oscillator is of the form:

$$\mathcal{L}(X) = 0$$

where \mathcal{L} is a linear operator acting on our system variables, X . A linear differential equation allows for the principle of superposition. If we have multiple solutions, u_1, u_2, \dots, u_n , linear combinations of said solutions, $u = (a_1u_1 + a_2u_2 + \dots + a_nu_n)$ are also a solution of the differential equation:

$$\mathcal{L}(u) = \mathcal{L}(a_1u_1 + a_2u_2 + \dots + a_nu_n) = a_1\mathcal{L}(u_1) + a_2\mathcal{L}(u_2) + \dots + a_n\mathcal{L}(u_n) = 0.$$

Linear superposition is a powerful mathematical tool that allows us to find analytical solutions of linear systems. However, nonlinearity breaks this property, and we can no longer exploit linear superposition to find general solutions to our differential equation [14]. As a consequence, there is no canonical, generalized method to studying nonlinear systems.

Linear oscillators have characteristics that are well studied and known. For example, they maintain their natural frequency independent of initial condition and oscillatory amplitude [14]. Thus, the oscillatory behavior of a solution can be assumed to be similar for initial conditions close to each other. This is another property that is broken by nonlinearity. A nonlinear oscillator can have solutions that depend on amplitude and are sensitive to initial conditions in the long run. This richness in solution dynamics coupled with a lack of standardized analysis methods make studying nonlinear oscillators a challenge. The decrease in phase drift error by inducing traveling wave patterns is a model independent concept. The theory is valid for any type of nonlinear oscillators. A few examples of nonlinear oscillators can be seen in the next sections.

2.1 DUFFING OSCILLATOR

The Duffing oscillator is a well known example of a nonlinear oscillator. Its canonical equation is:

$$\ddot{x} + \delta\dot{x} + \beta x + \alpha x^3 = \gamma \cos \omega t. \quad (2.1)$$

This is a second order, nonlinear differential equation. The δ parameter describes the damping strength applied to the system, $\gamma \cos \omega t$ models external forcing on the system, and the nonlinear term is αx^3 . We set $\gamma = 0$ to remove the forcing and simplify our analysis. Then, removing the damping parameter, δ , makes the system Hamiltonian. The energy potential for the case $\alpha > 0$ and for different parameters, δ and β , is given by Fig. 2.1.

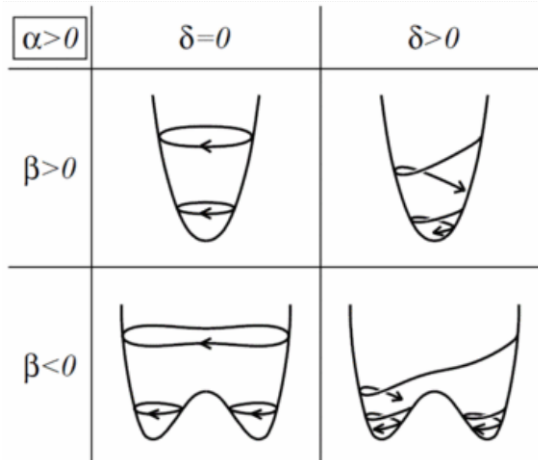


Figure 2.1. Energy potential for Duffing oscillator without forcing. As we can see, when we remove the damping parameter, $\delta = 0$, we have Hamiltonian system. The system has single-well potential for parameter $\beta > 0$ and a double-well potential for $\beta < 0$. Source: T. KANAMARU, *Duffing oscillator*, Scholarpedia, 3 (2008), p.6327. revision #91210.

At $\beta = 0$, the system undergoes a supercritical pitchfork bifurcation. For $\beta < 0$, this system has a single equilibrium point. The stability of this fixed point is dependent on the damping parameter, δ . For values $\beta > 0$, the system will now have three equilibrium points, as it undergoes a pitchfork bifurcation. In Fig. 2.2 we display different phase portraits for the Duffing oscillator without external forcing. Even though the original non-autonomous system has been simplified to an autonomous system, the oscillator still displays multiple, complex dynamics. Notably, the system can even display chaotic attractors as solutions.

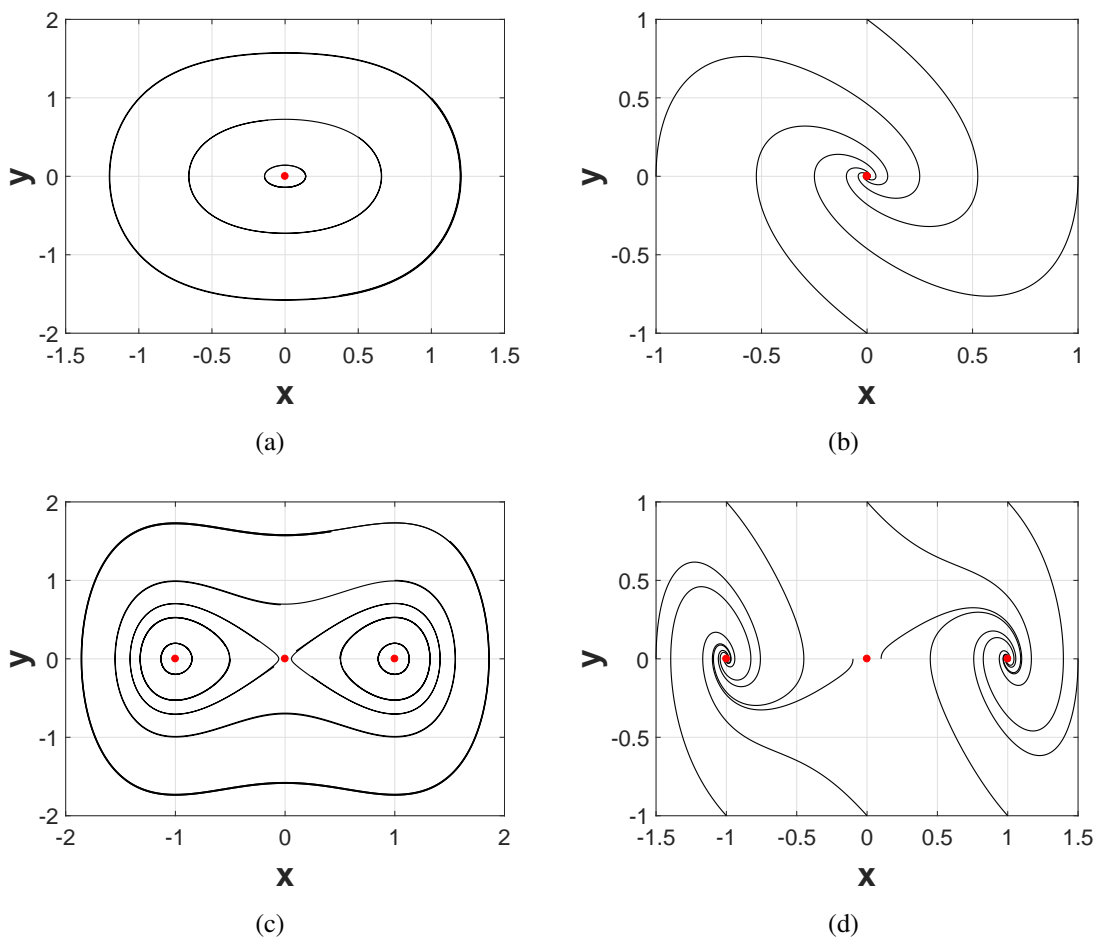


Figure 2.2. Undamped case (a) and damped case (b) for $\beta < 1$ with the single-well potential plot. Undamped case (c) and damped case (d) for $\beta > 1$ with the double-well potential plot. Panel (d) shows that the damped case converges to two different stable equilibria.

2.2 VAN DER POL OSCILLATOR

The Van der Pol Oscillator was proposed by Balthasar Van der Pol in 1920 [20]. It was originally used to model the “tetrode multivibrator” circuit used in early commercial radios [19]. The circuit diagram can be seen in Fig. 2.3.

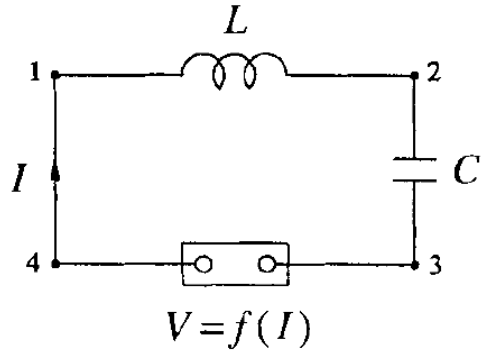


Figure 2.3. Circuit for the Van der Pol oscillator where its current-voltage characteristic, $V = f(I)$, resembles a cubic function. Source: S. STROGATZ, *Nonlinear Dynamics and Chaos: With Applications to Physics, Biology, Chemistry, and Engineering*, Studies in Nonlinearity, Avalon Publishing, 2014.

The equation for the Van der Pol oscillator is:

$$\ddot{x} - \epsilon(1 - x^2)\dot{x} + x = 0. \quad (2.2)$$

The nonlinearity appears in the damping term, $\epsilon(1 - x^2)$. To simplify the analysis, this second order differential equation can be changed into a system of first order differential equations.

By setting $F(x) = \frac{1}{3}x^3 - x$ and $w = \dot{x} + \mu F(x)$, the Van der Pol equation implies

$$\begin{aligned} \dot{x} &= w - \mu F(x), \\ \dot{w} &= -x \end{aligned} \quad (2.3)$$

and the change in variables $y = \frac{w}{\mu}$ leads to

$$\begin{aligned} \dot{x} &= \epsilon[y - F(x)], \\ \dot{y} &= -\frac{1}{\epsilon}x \end{aligned} \quad (2.4)$$

where $F(x) = \frac{1}{3}x^3 - x$ [19]. The system undergoes a Hopf bifurcation at $\epsilon = 1$ [19]. The equilibrium point changes from stable to unstable and a stable limit cycle is formed. Figure 2.4 shows a phase portrait of the limit cycle, $\epsilon \gg 1$ [19]. Figure 2.5 depicts the time-series solution of the limit cycle. The trajectory is an example of relaxation oscillations, with fast and slow changes occurring periodically in time.

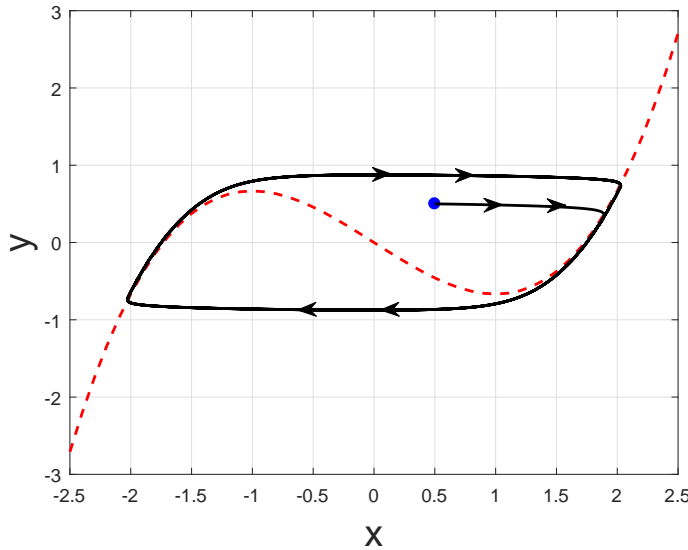


Figure 2.4. Phase plane of the Van der Pol oscillator with the variable transformation seen above and $\epsilon = 5$. We can see that it follows the trajectory of the cubic nullcline, $F(x)$, and quickly jumps horizontally once it reaches either of the local minima/maxima. These type of oscillations where we have a slow buildup followed by a quick discharge are called “relaxation oscillations.”

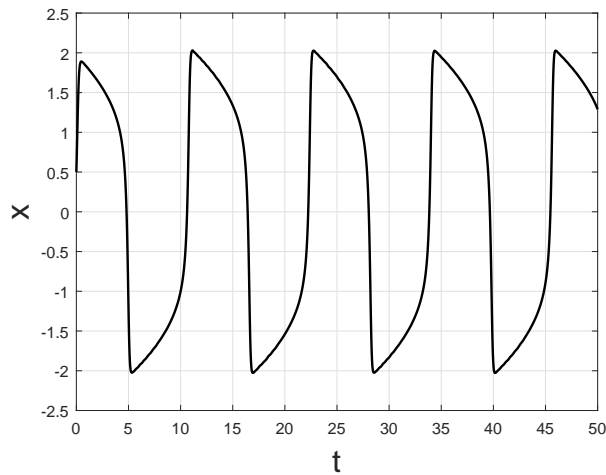


Figure 2.5. Solution of the Van der Pol system vs time. The characteristic “relaxation oscillations” can also be seen in this plot.

Not only is the Van der Pol oscillator useful in circuits and a classic pedagogical tool to study nonlinear oscillations, but modifications of it are used to study many types of natural oscillatory systems such as neurons. Similar to the Duffing oscillator, this apparently simple

system can exhibit very interesting and applicable behavior which further imparts the importance of studying these systems.

2.3 CRYSTAL OSCILLATORS

Crystals oscillators are another type of nonlinear oscillators with a wide range of applications. The quartz crystal oscillator is commonly used in clocks and other timing devices. As mentioned before, the purpose of studying NCCOs is to create a high precision timing device. Previous works had already considered networks of coupled crystal oscillators [4, 5]. However, crystal oscillators can typically operate over a limited range of frequencies, while Colpitts have a broader frequency band of operation. For this reason, we consider now networks of Colpitts oscillators.

Crystal quartz oscillators are often used in timing devices due to their accuracy. A quartz crystal distorts when an electric field is applied to an electrode near it. This effect is known as electrostriction or inverse piezoelectricity [16]. Once the field is removed, the crystal returns to its original shape and generates voltage. If we take advantage of this property of crystals, we can apply the voltage signal to the crystal resonator, amplify it, and feed it back to the resonator. This behavior is similar to a circuit with an inductor, capacitor, and resistor [16]. The setup of the quartz oscillator circuit can be seen Fig. 2.6.

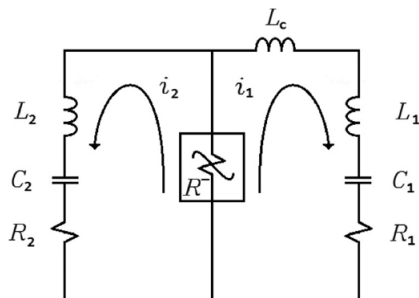


Figure 2.6. Circuit diagram for quartz crystal oscillators. This is a two-mode crystal oscillator circuit. A second set of RLC components are introduced by parasitic elements. Source: P. BUONO, B. CHAN, J. FERREIRA, A. PALACIOS, S. REEVES, P. LONGHINI, AND V. IN, *Symmetry-breaking bifurcations and patterns of oscillations in rings of crystal oscillators*, SIAM Journal on Applied Dynamical Systems, 17 (2018), pp. 1310-1352.

The resonant frequency of the circuit is determined by the cut and size of the crystal. Applying Kirchoff's law of voltage we get the following governing equations:

$$L_j \frac{d^2 i_j}{dt^2} + R_j \frac{di_j}{dt} + \frac{1}{C_j} i_j = [a - 3b(i_1 + i_2)^2] \left[\frac{di_1}{dt} + \frac{di_2}{dt} \right], \quad (2.5)$$

where $j = 1, 2$. As mentioned, networks of coupled quartz crystal oscillators have been used for the creation of a precision timing device similar to what is proposed in this paper. The networks of N coupled crystals oscillators also take advantage of the decrease in phase drift from $1/\sqrt{N}$ to $1/N$ gained by inducing a traveling wave (phase shift) behavior in the solution. Fig. 2.7 shows experimental measurements of the traveling wave pattern seen in a network of coupled crystal oscillators.

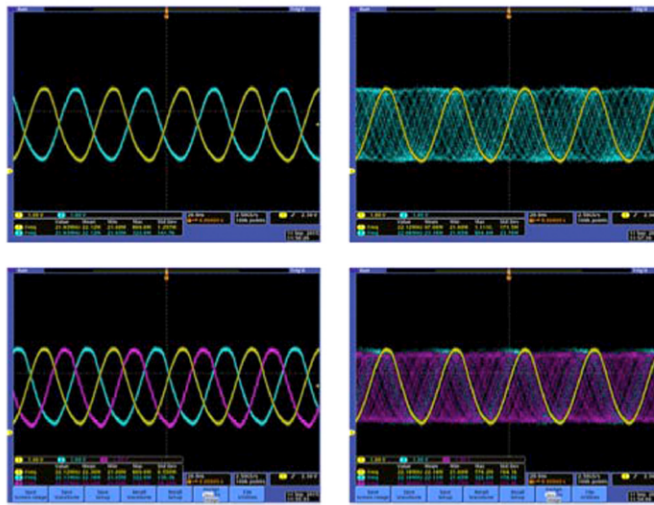


Figure 2.7. Experimental measurements for $N=2$ and $N=3$ oscillators revealing the predicted traveling wave pattern. Source: P. BUONO, B. CHAN, J. FERREIRA, A. PALACIOS, S. REEVES, P. LONGHINI, AND V. IN, *Symmetry-breaking bifurcations and patterns of oscillations in rings of crystal oscillators*, SIAM Journal on Applied Dynamical Systems, 17 (2018), pp. 1310-1352.

The study of networks of coupled crystal oscillators validated predictions that traveling wave patterns reduce the scaling error. Fig. 2.8 shows the significant decrease in scaling error seen in traveling wave solutions in comparison to the other type of solutions. While the research and experiments performed on the network of coupled crystal oscillators appeared promising, working with these type of oscillators present significant drawbacks. Not only is cutting and mounting the crystals not ideal from a manufacturing point of view, but once a quartz crystal is cut and mounted, the system can only work in a very small range of frequencies. This makes production and robustness an issue, and one goal of this new precision timing device is to have high accuracy along with potential for mass production and robustness in all types of

environments. Thus, we consider replacing the quartz crystal oscillator with a Colpitts oscillator.

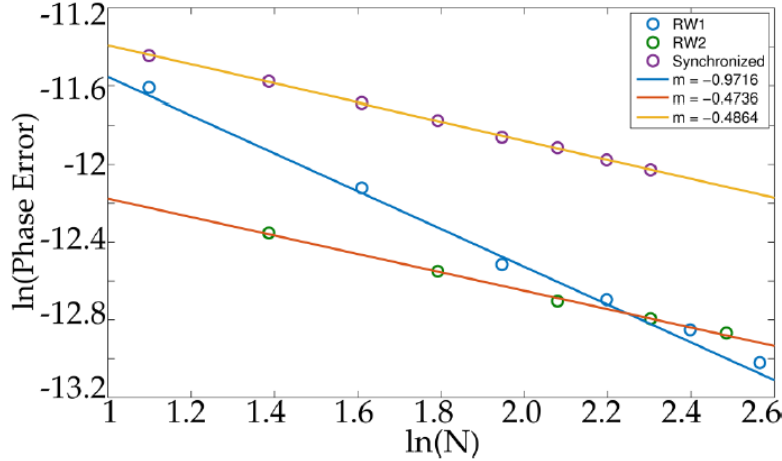


Figure 2.8. Log scaled phase error vs N for RW1 type solutions: Traveling Wave also known as phase drift by T/N solutions; RW2 solutions: phase drift by $T/2$ solutions; and Synchronized, fully in phase solutions. A least squared regression line is fit to data for each different solution type. Source: P. BUONO, B. CHAN, J. FERREIRA, A. PALACIOS, S. REEVES, P. LONGHINI, AND V. IN, *Symmetry-breaking bifurcations and patterns of oscillations in rings of crystal oscillators*, SIAM Journal on Applied Dynamical Systems, 17 (2018), pp. 1310-1352.

2.4 COLPITTS OSCILLATOR: CIRCUIT MODEL

The Colpitts oscillator offers a solution to the aforementioned problem. This oscillator is a parallel LC circuit that was designed to be an almost sinusoidal oscillator [18]. This sinusoidal feedback is caused by a capacitance divider along with its inductance component [18]. The circuit diagram of the Colpitts oscillator used for this application can be seen in Fig. 2.9.

This circuit is simple to manufacture and displays rich dynamical behavior at different parameter values [6]. In order to perform our analysis, Kirchoff's voltage law is used to model the circuit with the following governing equations:

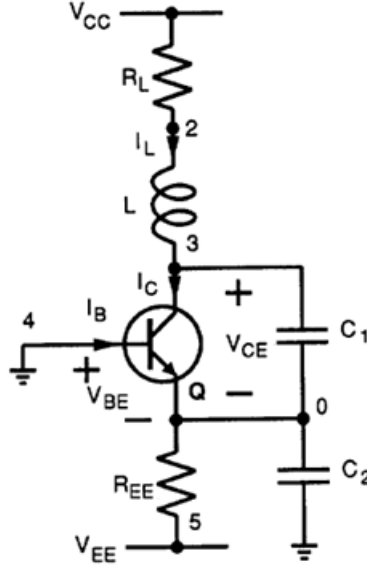


Figure 2.9. Single Colpitts Circuit Diagram .

$$\begin{aligned}
 \frac{dV_C}{dt} &= \frac{I_L - I_C}{C_1} + \frac{\frac{V_{EE} + V_B - V_E}{R_{EE}} + I_L + I_B}{C_2}, \\
 \frac{dV_E}{dt} &= \frac{\frac{V_{EE} + V_B - V_E}{R_{EE}} + I_L + I_B}{C_2}, \\
 \frac{dI_L}{dt} &= \frac{V_{CC} - V_C + V_B - I_L R_L}{L},
 \end{aligned} \tag{2.6}$$

where

$$I_B = \begin{cases} 0 & \text{if } V_B - V_E \leq V_{TH} \\ \frac{V_B - V_E - V_{TH}}{R_{ON}} & \text{if } V_B - V_E > V_{TH} \end{cases}$$

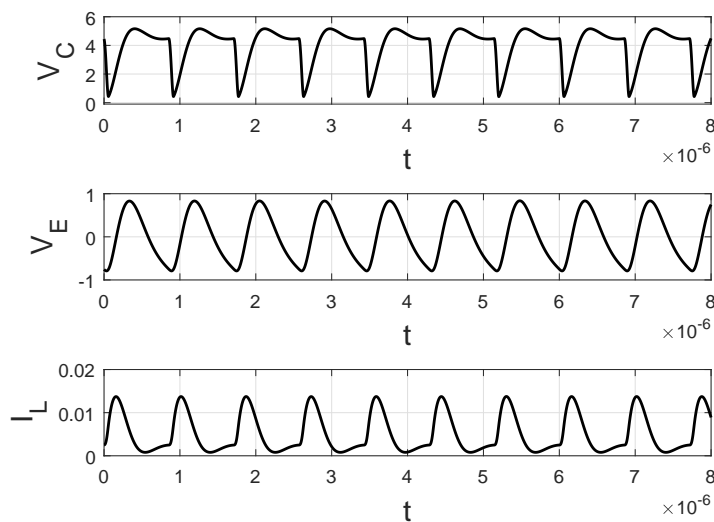
$$I_C = \beta I_B.$$

These equations model the BJT transistor. Here, V_C is the collector voltage, V_E is the emitter voltage, and I_L represents the current. The piecewise-linear equation I_B , and consequently I_C , is used to model the current of the BJT transistor seen in the circuit diagram [13]. In this context, V_{TH} is the threshold voltage and β is the forward current gain. Effectively, the BJT works as a cutoff and forward active element in the current [13]. The parameter values are shown in Table 2.1.

Figs. 2.10 and 2.11 display numerical solutions of the Colpitts oscillator system of equations.

Table 2.1. Colpitts Oscillator Circuit Parameters .

Parameter	Value
V_{CC}	5 V
R_L	200 Ω
L	21.8e-6 H
C_1	1e-9 F
C_2	1e-9 F
R_{EE}	1000 Ω
V_{EE}	-5 V
β	260
R_{ON}	100 Ω
V_{TH}	0.75 V
V_B	0 V

**Figure 2.10. Solution of the system vs time of all three system components of circuit equations.**

For the sake of our precision timing applications, we focus primarily on solution regions where the system exhibits single period, near sinusoidal oscillations. These type of solutions can be seen in Fig. 2.10, specifically in the oscillations displayed by the emitter voltage, V_E .

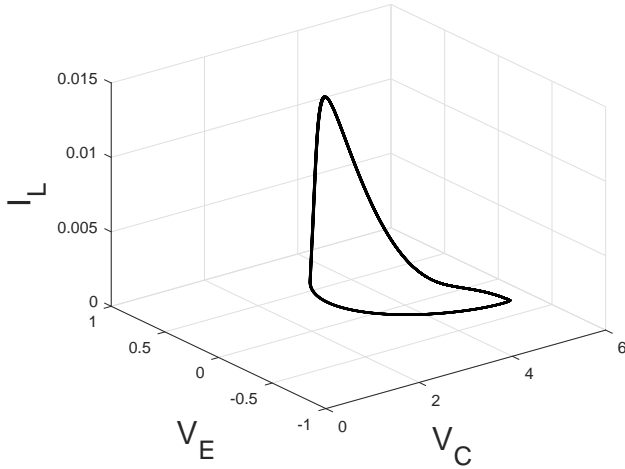


Figure 2.11. Solution phase plane for all three system components.

2.5 COLPITTS OSCILLATOR: IDEAL MODEL

Eq. (2.6) were obtained by modeling the Colpitts oscillator circuit diagram using Kirchoff's laws of voltage. These equations will be used to pinpoint ideal parameter ranges that directly relate to the timing device being built. However, to simplify our bifurcation analysis, we will study the normal form of Eq. (2.6); see Ref. [19] for details on this practice. These normal form equations have been reduced and non-dimensionalized such that the principal dynamics of the system remain the same. Following Ref. [9], the normal form equations are:

$$\begin{aligned} \frac{dx_1}{dt} &= \frac{g}{Q(1-\kappa)} \left[-\left(e^{-x_2} - 1\right) + x_3 \right] \\ \frac{dx_2}{dt} &= \frac{g}{Q\kappa} x_3 \\ \frac{dx_3}{dt} &= -\frac{Q\kappa(1-\kappa)}{g} (x_1 + x_2) - \frac{1}{Q} x_3. \end{aligned} \tag{2.7}$$

The literature states the existence of oscillatory solutions for parameter values $g > 1$ and $Q > 0$ where κ is a scaling factor [9]. Refer to [6] and [9] for an in-depth analysis of the various oscillatory dynamics that arise in the system. Since these equations are meant as a reduced model of a physical problem, we let $Q > 0$. Fig. 2.12 shows the solution to the ideal model vs time. We validate the existence of a Hopf bifurcation at $g = 1$ by performing stability and bifurcation analysis.

We begin by linearizing the system which yields the Jacobian matrix:

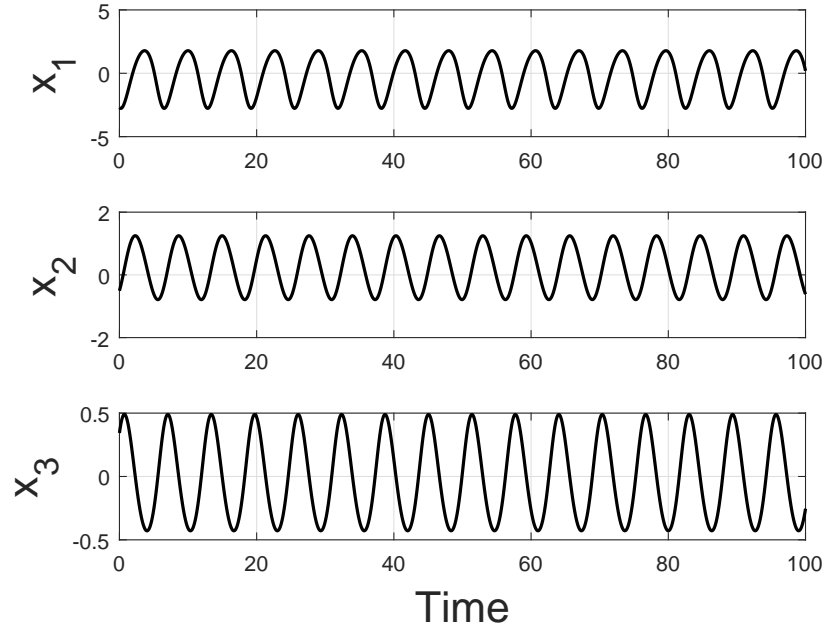


Figure 2.12. Solution of the ideal model system vs time. $g = 1.1$, $Q = 1$, and $\kappa = .5$. Note the difference in time scaling and simplification of oscillations when compared to the circuit model.

$$J = \begin{bmatrix} 0 & \frac{g}{Q(1-k)} e^{-x_2} & \frac{g}{Q(1-k)} \\ 0 & 0 & \frac{g}{Qk} \\ -\frac{Qk(1-k)}{g} & -\frac{Qk(1-k)}{g} & -\frac{1}{Q} \end{bmatrix}. \quad (2.8)$$

Evaluating this Jacobian matrix at $(0, 0, 0)$ yields:

$$J_{(0,0,0)} = \begin{bmatrix} 0 & \frac{g}{Q(1-k)} & \frac{g}{Q(1-k)} \\ 0 & 0 & \frac{g}{Qk} \\ -\frac{Qk(1-k)}{g} & -\frac{Qk(1-k)}{g} & -\frac{1}{Q} \end{bmatrix}. \quad (2.9)$$

To determine the stability of the system we calculate the eigenvalues of the system:

$$|J - \sigma I| = 0, \quad (2.10)$$

which leads to

$$\sigma^3 + \frac{1}{Q}\sigma^2 + \sigma + \frac{g}{Q} = 0. \quad (2.11)$$

The determinant leaves us with a cubic polynomial represented by Eq. (2.11). At $g = 1$, the eigenvalues are $\sigma_1 = -\frac{1}{Q}$ and $\sigma_{2,3} = 0 \pm i$. Since we are interested in the Hopf bifurcation that occurs at $g = 1$, we perform the next asymptotic expansion of the eigenvalues around the Hopf bifurcation point $g = 1$. So, we let $g = 1 + \epsilon$ where $\epsilon \ll 1$ is a small perturbation such that $\epsilon = g - 1$. Consider $\sigma_1 = -\frac{1}{Q} + a_1\epsilon$. Subbing σ_1 into Eq. (2.11) yields:

$$\left(-\frac{1}{Q} + a_1\epsilon\right)^3 + \frac{1}{Q} \left(-\frac{1}{Q} + a_1\epsilon\right)^2 + \left(-\frac{1}{Q} + a_1\epsilon\right) + \frac{1}{Q}(1 + \epsilon) = 0$$

By collecting like powers of ϵ up to first order, we get

$$\begin{aligned} \left(\frac{3a_1}{Q^2} - \frac{2a_1}{Q^2 + a_1} + \frac{1}{Q}\right)\epsilon + \mathcal{O}(\epsilon^2) &= 0 \\ \frac{a_1}{Q^2} + a_1 + \frac{1}{Q} &= 0. \end{aligned}$$

Solving for a_1 leads to:

$$a_1 = -\frac{Q}{Q^2 + 1}.$$

We now substitute our value of a_1 (with $\epsilon = g - 1$) into $\sigma_1 = -\frac{1}{Q} + a_1\epsilon$ to obtain the real eigenvalue:

$$\sigma_1 = -\frac{1}{Q} - \frac{Q}{Q^2 + 1}(g - 1),$$

which can be written as:

$$\sigma_1 = -\frac{1 + gQ^2}{Q(Q^2 + 1)}. \quad (2.12)$$

Now consider our complex conjugate pair, $\lambda_{2,3}$, and perform the same perturbation technique by substituting $\sigma_{2,3} = \pm i + a_2\epsilon$ into Eq. 2.11 which yields:

$$(i + a_2\epsilon)^3 + \frac{1}{Q}(i + a_2\epsilon)^2 + (i + a_2\epsilon) + \frac{1}{Q}(1 + \epsilon) = 0.$$

By collecting like powers of ϵ up to order one, we get

$$-i + \left(-3a_2 + \frac{2a_2}{Q}i + a_2 + \frac{1}{Q}\right)\epsilon - \frac{1}{Q} + i + \frac{1}{Q} = 0.$$

The system is now solved for our value of a_2 , which yields

$$a_2 = \frac{Q}{2(Q^2 + 1)} + \frac{1}{2(Q^2 + 1)i}.$$

Substituting back into $\sigma_{2,3} = \pm i + a_2\epsilon$ leads to,

$$\sigma_{2,3} = \frac{Q}{2(Q^2 + 1)}(g - 1) \pm \left[1 + \frac{1}{2(Q^2 + 1)}(g - 1) \right] i. \quad (2.13)$$

If we look at the complex conjugate pair of eigenvalues $\sigma_{2,3}$, we see that $\text{Re}(\sigma_{2,3}) = 0$ at $g = 1$, which implies a crossing of the imaginary axis. This is a Hopf bifurcation validating the existence of oscillatory solutions for values $g > 1$ seen in Refs. [6] and [9].

The numerical continuation tool *AUTO* is used to further illustrate these results. A detailed bifurcation plot can be seen in Fig. 2.13. Stable limit cycles emerge right after the Hopf bifurcation. The system then undergoes period doubling bifurcation cascades as we move farther away from $g = 1$. These oscillations are near sinusoidal for values near the Hopf bifurcation. This result can be seen in Figs. 2.12 and 2.14. A more detailed description of the systems complex behavior away from the Hopf bifurcation can be seen in Refs. [6] and [9]. The analysis on our reduced, phenomenological model validates the existence of stable limit cycles which are crucial in timing devices. Throughout the rest of this thesis, we analyze systems of this Colpitts Oscillator coupled unidirectionally.

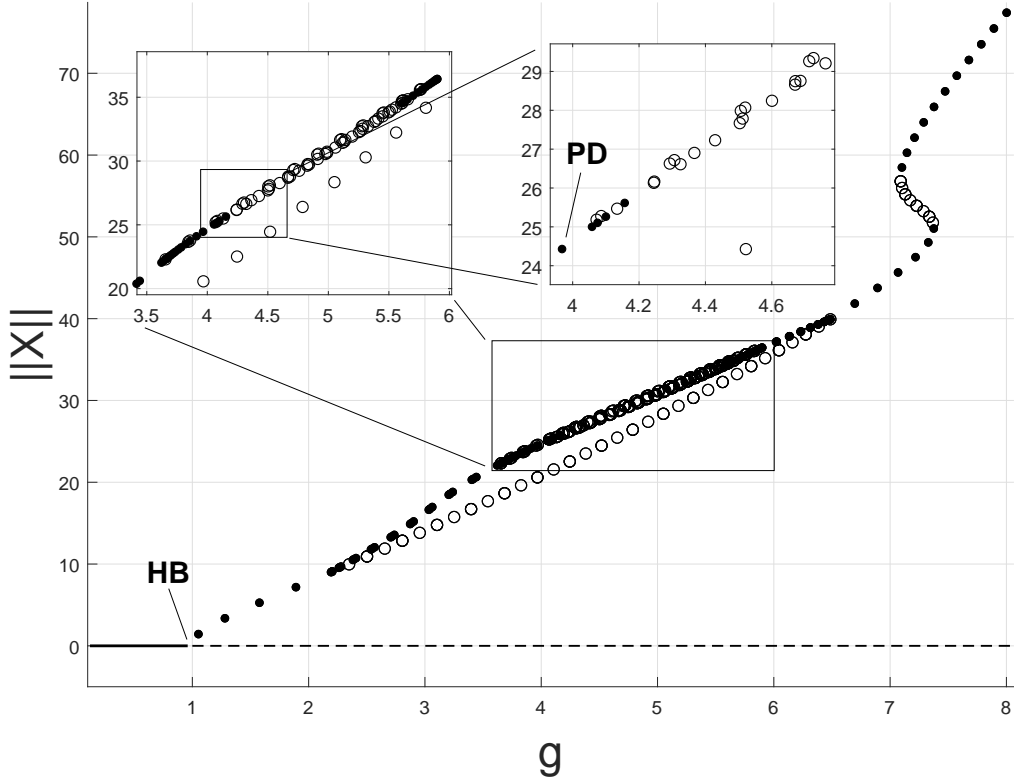


Figure 2.13. One-parameter bifurcation diagram of a reduced model for a Colpitts oscillator. Solid lines represent stable equilibria, dashed lines represent unstable equilibria, filled-in circles represent stable orbits, and empty circles represent unstable orbits. We see the emergence of stable limit cycles at the Hopf bifurcation at $g = 1$. These stable limit cycles remain quasi-sinusoidal until the emergence of period doubling at approximately $g = 4$. A cascade of period doubling not detailed in the plot emerges in the vicinity of the first period doubling bifurcation. This period doubling behavior reverts and re-emerges as g increases and moves away from the Hopf bifurcation.

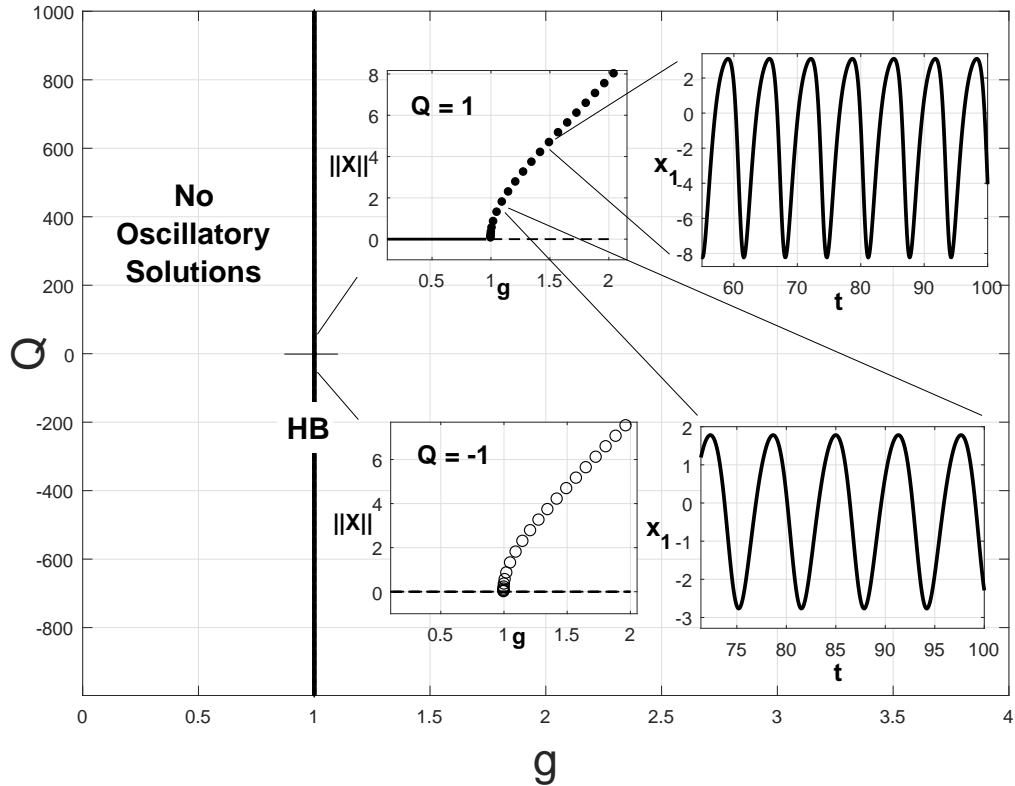


Figure 2.14. Two-parameter bifurcation diagram of a reduced model for a Colpitts Oscillator. A Hopf locus persist at $g = 1$ for all values of Q . The Hopf locus is traced by a vertical, solid line. For values of $Q < 0$ a Hopf bifurcation at $g = 1$ leads to unstable limit cycles. The physically relevant case, $Q > 0$, has a Hopf bifurcation at $g = 1$, which produces stable limit cycles. These two cases are seen in the subfigures plotting the norm of the system, $\|X\|$, vs values of g . Dashed lines represent unstable equilibrium points; solid lines represent stable equilibria; empty circles denote unstable limit cycles; closed circles represent stable limit cycles. The stable limit cycles become more sinusoidal as g is chosen near the Hopf point. This can be seen in the subfigures showing the time solution of the first component vs time.

CHAPTER 3

NETWORK OF UNIDIRECTIONALLY COUPLED COLPITTS OSCILLATORS: CIRCUIT MODEL

In this section we extend the theory and governing equations of a Colpitts oscillator to a network of CCO. We assume that all Colpitts oscillators are identical and coupled unidirectionally in a ring fashion, as is seen in Fig 3.1. This form of coupling leads to a network with \mathbb{Z}_N symmetry, where \mathbb{Z}_N is the group of cyclic permutations of N objects. In this case, the objects are individual oscillators.

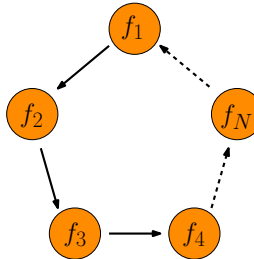


Figure 3.1. Concept diagram for network of N coupled oscillators .

3.1 GOVERNING EQUATIONS

In our model, the coupling is determined by Kirchoff's voltage law which leads to linear coupling terms. We assume the coupling between oscillators to be identical and instantaneous. The governing equations for a Network of CCO are:

$$\begin{aligned}
 \frac{dV_{Cn}}{dt} &= \frac{I_{Ln} - I_{Cn}}{C_1} + \frac{\frac{V_{EE}+V_B-V_{En}}{R_{EE}} + I_{Ln} + I_{Bn}}{C_2} + \frac{\lambda}{C_1 R_{EE}} (V_{C_{n+1}} - V_{C_n}), \\
 \frac{dV_{En}}{dt} &= \frac{\frac{V_{EE}+V_B-V_{En}}{R_{EE}} + I_{Ln} + I_{Bn}}{C_2}, \\
 \frac{dI_{Ln}}{dt} &= \frac{V_{CC} - V_{Cn} + V_B - I_{Ln} R_L}{L},
 \end{aligned} \tag{3.1}$$

where

$$I_{Bn} = \begin{cases} 0 & \text{if } V_B - V_{En} \leq V_{TH} \\ \frac{V_B - V_{En} - V_{TH}}{R_{ON}} & \text{if } V_B - V_{En} > V_{TH} \end{cases}$$

$$I_{Cn} = \beta I_{Bn}.$$

These equations are a variation of the uncoupled, single Colpitts oscillator circuit model. The unidirectional coupling term obtained from Kirchoff's law couples the capacitor voltage, C_1 , between oscillators. The coupling between different voltage portions of the system equations is denoted as: $\frac{\lambda}{C_1 R_{EE}} (V_{C_{n+1}} - V_{C_n})$. The new parameter introduced, λ , is a dimensionless unit denoting the coupling strength between oscillators and is meant to allow for changes in the resistance of the coupling components. In the next section, we look at the system's inherent symmetry to predict all possible solution patterns.

3.2 CONSEQUENCES OF SYMMETRY

Systems of unidirectionally coupled oscillators exhibit spatio-temporal symmetry denoted by the group $\Gamma = \mathbb{Z}_N \times S^1$. \mathbb{Z}_N is rotational symmetry and S^1 the circle group of phase shifts acting on 2π -periodic functions [12]. This implies that a system

$$\frac{dX}{dt} = F(X) \quad (3.2)$$

where $X(t)$ is a solution with period of approximately 2π , has the property

$$(\gamma, \theta) \cdot X(t) \equiv \gamma X(t + \theta) = X(t), \quad \forall t, \quad (3.3)$$

with $(\gamma, \theta) \in (\mathbb{Z}_N \times S^1)$. Now, let $L = (df)_{\vec{x}=0}$ be the linearization of the system about the trivial solution with a pair of eigenvalues crossing the imaginary axis, $\pm i\omega$. This implies that the eigenspace $E_{i\omega}$ is the sum of two absolutely irreducible representations or is a non-irreducible representation. This is known as a Γ -simple representation [11, 12]. The analysis is simplified, without loss of generality, by assuming the frequency of our system is $\omega = 1$.

If we have a generator $\gamma \in \mathbb{Z}_N$, then it acts irreducibly by complex rotations on $z \in \mathbb{C}$: $\gamma \cdot z = \zeta^m \cdot z$ where $m = 0, \dots, N - 1$ and $\zeta^m = e^{m2\pi i/N}$. Note that if $m = 0$, $\zeta^0 = 1 \implies \gamma \cdot z = z$ which is the trivial representation. If $m = N/2$ (N is even), $\zeta^{N/2} = e^{i\pi} \implies \gamma \cdot z = -z$ which is the alternating representation. We denote these irreducible representations by V_m for $m = 0, \dots, 1$ which form the isotypic decomposition:

$$\mathbb{R}^N = V_0 \oplus V_1 \oplus \dots \oplus V_m \oplus \dots \oplus V_{N-1}. \quad (3.4)$$

Each irreducible representation V_m denotes a fixed-point subspace, Σ_m . The eigenspace, E_i , generically corresponds to an irreducible representation, V_m , where we must allow the action of phase shift symmetries, $\theta \in S^1$ where

$$\theta \cdot z = e^{i\theta} z. \quad (3.5)$$

So, the group $\Gamma = \mathbb{Z}_N \cdot S^1$ acts on E_i via

$$(\gamma, \theta) \cdot z = \zeta^m \cdot e^{i\theta} \cdot z = e^{im2\pi/N} \cdot e^{i\theta} \cdot z. \quad (3.6)$$

The irreducible representation is fixed by the group

$$\begin{aligned} \Sigma_m &= \{(\gamma^k, \theta) : (\zeta^m)^k e^{i\theta} = 1\} \\ &= \{(\gamma^k, \theta) : e^{\frac{2\pi mk}{N} + \theta} i = 1\} \\ &= \{(\gamma^k, \theta = -\frac{2\pi mk}{N}) | k = 0, \dots, N-1\} \subset \mathbb{Z}_N \times S^1. \end{aligned}$$

with

$$\bar{\mathbb{Z}}_{N/d} = (\Sigma_m \cap \mathbb{Z}_N) = \{(-2\pi km, \gamma^k) | k = 0, \dots, N-1\}. \quad (3.7)$$

where $\bar{\mathbb{Z}}_{N/d} \simeq \mathbb{Z}_{N/d}$ and $d = \gcd(m, N)$. The Equivariant Hopf Theorem (EHT) guarantees the following.

Suppose the linearization of our system, $(df)_{\vec{x}=0}$, at the trivial solution has a pair of complex conjugate eigenvalues crossing the imaginary axis at $\pm i$. Then, EHT guarantees a unique branch of periodic solutions with period of approximately 2π bifurcating from the trivial equilibrium, and the symmetry group of the periodic solution is given by the pair $(H, K) = (\Sigma_m, \bar{\mathbb{Z}}_{N/d})$ where $H/K \simeq S^1$. K is the subgroup of purely spatial symmetries that fix a periodic solution, $X(t)$, at every point in time,

$$K = \{\gamma \in \Gamma : \gamma X(t) = X(t), \forall t\}. \quad (3.8)$$

H is the group that fixes the trajectory of $X(t)$ but not necessarily the phases. This group is defined as

$$H = \{\gamma \in \Gamma : \gamma \{X(t)\}, \forall t\} \quad (3.9)$$

and is responsible for temporal phase shifts that a solution can exhibit. Therefore, the periodic solution is a rotating wave with $\bar{\mathbb{Z}}_{N/d}$ spatial symmetry. The waveforms guaranteed by the EHT are now described. Let

$$X(t) = (x_1(t), \dots, x_N(t)) \quad (3.10)$$

be a rotating wave with symmetry $(\Sigma_m, \bar{\mathbb{Z}}_{N/d})$. The effect of the elements of the form $(1, -\theta)$ on $X(t)$ guarantee that we have rotating waves,

$$e^{-i\theta} x_j(t) = x_j(t - \theta) \quad (3.11)$$

for $j = 1, \dots, N$. The spatial symmetry action on $X(t)$ is given by,

$$(-2\pi m/N, \gamma) \cdot X(t) = (e^{-2\pi im/N} x_2(t), e^{-2\pi im/N} x_3(t), \dots, e^{-2\pi im/N} x_1(t)), \quad (3.12)$$

$$\text{so, } \left(-\frac{2\pi m}{N}, \gamma\right) \cdot X(t) = X(t)$$

$$\implies X(t) = (X_{(N/d)1}(t), \dots, X_{(N/d)d}(t)). \quad (3.13)$$

This means there are d blocks of rotating waves with the pattern $\forall j = 1, \dots, d$,

$$X_{(N/d)j}(t) = \left(x_1(t), x_1\left(t + \frac{2\pi m}{N}\right), \dots, x_1\left(t + \frac{2\pi((N/d)-1)m}{N}\right) \right)$$

where the phase shifts are taken $\mod (2\pi)$.

Example 3.2.1. Consider the case $N = 6$ with $m = 3$ which implies $d = 3$. This case has a parameter family of rotating waves with isotropy subgroup $(\Sigma_3, \bar{\mathbb{Z}}_2) \equiv (\mathbb{Z}_4, \mathbb{Z}_2)$. Formula 3.13 gives the pattern:

$$X(t) = (x_1(t), x_1(t + \pi), x_1(t), x_1(t + \pi), x_1(t), x_1(t + \pi)).$$

This type of rotating wave pattern is referred to as a variant of a standing wave (SW) solution. The pattern is better visualized in Fig. 3.2.

This generalized approach allows us to find all possible patterns that arise as a consequence of the symmetry in a system of unidirectionally coupled oscillators. We now apply this approach to the cases $N = 3 - 6$.

Let T correspond to the period of an oscillating solution. We employ the notation $\gamma^m = \langle \frac{mT}{N} \rangle \equiv e^{mTi/N}$ to denote our generators. The patterns guaranteed by the EHT are seen in Table 3.1. Symmetry group $(H, K) = (\mathbb{Z}_3, \mathbb{Z}_3)$ produces the trivial, or in phase (IP), pattern where all oscillators display the same solution, $x_1(t)$, and no phase shift. Figure 3.3 shows the IP pattern that emerges in our system of equations. Symmetry group $(H, K) = (\mathbb{Z}_3, \mathbb{1})$ produces the rotating wave referred to as the traveling wave (TW). This wave pattern can also be generated by $\gamma^2 = \langle \frac{2T}{3} \rangle$ which changes the direction of the phase shift,

$$TW := X(t) = \left(x_1(t), x_1\left(t + \frac{2T}{3}\right), x_1\left(t + \frac{T}{3}\right) \right).$$

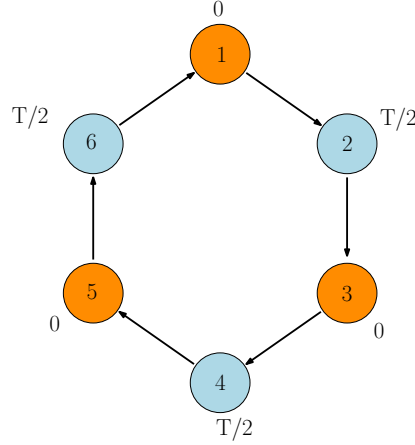


Figure 3.2. Network of six oscillators coupled unidirectionally.
Same colored nodes represent in phase oscillations. Every oscillator is labeled with its respective phase shift generated by $\gamma^3 = \langle \frac{T}{2} \rangle$ where T is the oscillator's period.

Table 3.1. Symmetry Groups: N=3 .

γ	H	K	Wave Pattern
$\gamma^0 = \langle 1 \rangle$	\mathbb{Z}_3	\mathbb{Z}_3	$(x_1(t), x_1(t), x_1(t))$
$\gamma^1 = \langle \frac{T}{3} \rangle$	\mathbb{Z}_3	$\mathbb{1}$	$(x_1(t), x_1(t + \frac{T}{3}), x_1(t + \frac{2T}{3}))$
	$\mathbb{1}$	$\mathbb{1}$	$(x_1(t), x_2(t), x_3(t))$

The TW pattern is observed in our system of equations and is seen in Fig. 3.4. Symmetry group $(H, K) = (\mathbb{1}, \mathbb{1})$ denotes loss of all symmetry. All wave solutions are unrelated to each other. In our model, this solution branch is populated by quasi-periodic (QP) solutions.

Case $N = 4$ produces the same qualitative solutions as $N = 3$. However, similar to Example 3.2.1., the symmetry group $(H, K) = (\mathbb{Z}_4, \mathbb{Z}_2)$ corresponds to SW type solutions with wave pattern as seen in Table 3.2. The SW wave pattern for $N = 4$ can be visualized with the diagram in Fig. 3.5. These rotating wave solutions appear when $d > 1$.

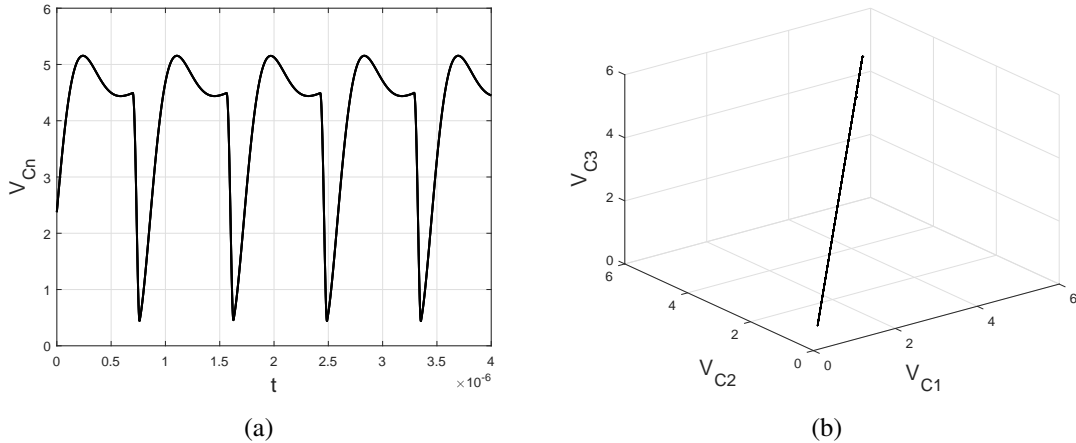


Figure 3.3. IP behavior for $N = 3$ for (3.1). Solution for voltage component, V_C , of three CCO with coupling strength $\lambda = 0.1$ (a). We can see a complete overlap of solutions between the three oscillators which indicates perfect IP behavior. Phase diagram of V_C solutions for all three CCOs with coupling strength value $\lambda = 0.1$ (b). The straight line shows complete IP synchronization between the three oscillators.

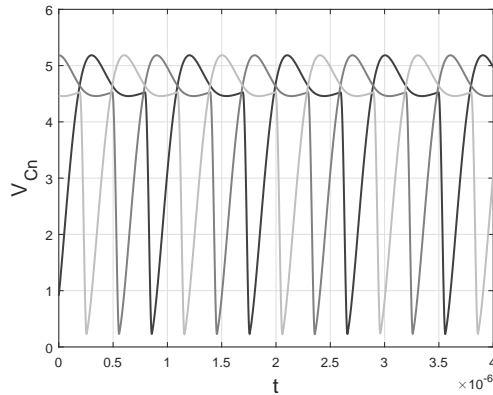


Figure 3.4. TW behavior for NCCOs with three oscillators. Solution for V_C component vs time for three CCOs at $\lambda = -0.1$. We can see the phase shift synchronization between oscillator.

Table 3.2. Symmetry Groups: N=4 .

γ	H	K	Wave Pattern
$\gamma^0 = \langle 1 \rangle$	\mathbb{Z}_4	\mathbb{Z}_4	$(x_1(t), x_1(t), x_1(t), x_1(t))$
$\gamma^1 = \langle \frac{T}{4} \rangle$	\mathbb{Z}_4	$\mathbb{1}$	$(x_1(t), x_1(t + \frac{T}{4}), x_1(t + \frac{T}{2}), x_1(t + \frac{3T}{4}))$
$\gamma^2 = \langle \frac{T}{2} \rangle$	\mathbb{Z}_4	\mathbb{Z}_2	$(x_1(t), x_1(t + \frac{T}{2}), x_1(t), x_1(t + \frac{T}{2}))$
	$\mathbb{1}$	$\mathbb{1}$	$(x_1(t), x_2(t), x_3(t), x_4(t))$

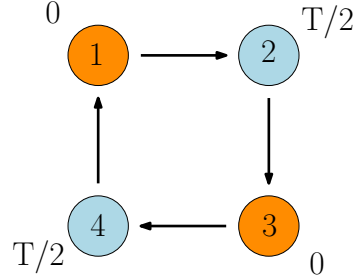


Figure 3.5. Network of four oscillators coupled unidirectionally. Same colored nodes represent in phase oscillations. Every oscillator is labeled with its respective phase shift generated by $\gamma^2 = \langle \frac{T}{2} \rangle$ where T is the oscillator's period.

The symmetry groups for $N = 5$ are listed in Table 3.3. Note that there are two rows listed for $(H, K) = (\mathbb{Z}_5, \mathbb{1})$ that have distinct patterns and generators. This is a property of oscillator networks with odd N .

Table 3.3. Symmetry Groups: N=5 .

γ	H	K	Wave Pattern
$\gamma^0 = \langle 1 \rangle$	\mathbb{Z}_5	\mathbb{Z}_5	$(x_1(t), x_1(t), x_1(t), x_1(t), x_1(t))$
$\gamma^1 = \langle \frac{T}{5} \rangle$	\mathbb{Z}_5	$\mathbb{1}$	$(x_1(t), x_1(t + \frac{T}{5}), x_1(t + \frac{2T}{5}), x_1(t + \frac{3T}{5}), x_1(t + \frac{4T}{5}))$
$\gamma^2 = \langle \frac{2T}{5} \rangle$	\mathbb{Z}_5	$\mathbb{1}$	$(x_1(t), x_1(t + \frac{2T}{5}), x_1(t + \frac{4T}{5}), x_1(t + \frac{T}{5}), x_1(t + \frac{3T}{5}))$
	$\mathbb{1}$	$\mathbb{1}$	$(x_1(t), x_2(t), x_3(t), x_4(t), x_5(t))$

The possible patterns that can be seen for $N = 6$ coupled oscillators is given by the group symmetries listed in Table 3.4. As illustrated in Example 3.2.1, there exists a symmetry group $(H, K) = (\mathbb{Z}_6, \mathbb{Z}_2)$ corresponding to a SW pattern. The table showing the possible solutions of a system with $N = 6$ oscillators displays another variant of the SW as a consequence of the group $(H, K) = (\mathbb{Z}_6, \mathbb{Z}_3)$ generated by γ^2 . This pattern is illustrated in Fig. 3.6.

This approach of using the system's inherent symmetry as a tool to predict possible solutions is model-independent. This is especially powerful as we have just proven that networks of oscillators coupled unidirectionally must go through symmetry breaking bifurcations that guarantee the sought TW solution. However, the EHT does not specify that solution branches emerging from symmetry breaking bifurcations must contain stable periodic orbits. Thus, the system must be studied further to verify whether the patterns

predicted are stable or not. In the next section, numerical bifurcation analysis is used to validate the analysis performed on the symmetry of the system.

Table 3.4. Symmetry Groups: N=6 .

γ	H	K	Wave Pattern
$\gamma^0 = \langle 1 \rangle$	\mathbb{Z}_6	\mathbb{Z}_6	$(x_1(t), x_1(t), x_1(t), x_1(t), x_1(t), x_1(t))$
$\gamma^1 = \langle \frac{T}{6} \rangle$	\mathbb{Z}_6	$\mathbb{1}$	$(x_1(t), x_1\left(t + \frac{T}{6}\right), x_1\left(t + \frac{T}{3}\right), x_1\left(t + \frac{T}{2}\right), x_1\left(t + \frac{2T}{3}\right), x_1\left(t + \frac{5T}{6}\right))$
$\gamma^2 = \langle \frac{T}{3} \rangle$	\mathbb{Z}_6	\mathbb{Z}_2	$(x_1(t), x_1(t + \frac{T}{3}), x_1(t + \frac{2T}{3}), x_1(t), x_1(t + \frac{T}{3}), x_1(t + \frac{2T}{3}))$
$\gamma^3 = \langle \frac{T}{2} \rangle$	\mathbb{Z}_6	\mathbb{Z}_3	$(x_1(t), x_1(t + \frac{T}{2}), x_1(t), x_1(t + \frac{T}{2}), x_1(t), x_1(t + \frac{T}{2}))$
	$\mathbb{1}$	$\mathbb{1}$	$(x_1(t), x_2(t), x_3(t), x_4(t), x_5(t))$

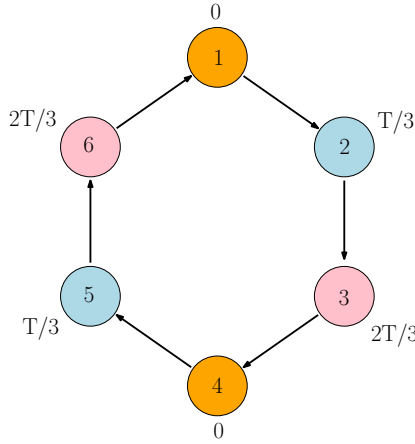


Figure 3.6. Network of six oscillators coupled unidirectionally. Same colored nodes represent in phase oscillations. Every oscillator is labeled with its respective phase shift generated by $\gamma^2 = \langle \frac{T}{3} \rangle$ where T is the oscillator's period.

3.3 COMPUTATIONAL BIFURCATION ANALYSIS

This section contains the numerical bifurcation analysis of the system with oscillator cases $N = 3$ to $N = 6$. The Circuit Model numerical analysis is used to study the qualitative behavior of the oscillator array as we vary parameter values and verify the existence and stability of the solution branches that emerge from the system's $\Gamma = (\mathbb{Z}_N, S^1)$ symmetry. The

practical purpose of this numerical work is to find regions where the system exhibits TW solutions. The numerical continuation tool, *AUTO*, is used to perform this analysis [7, 8].

We now look at the case of an array with $N=3$ coupled oscillators. Fig. 3.7 shows the bifurcation diagram for the Circuit Model equations as a function of the coupling strength, λ . The other parameters are held fixed. As a convention, dashed line represents unstable equilibrium points, empty circles represent unstable orbits, and filled-in circles represent stable orbits. Bold crosses denote Hopf bifurcation points.

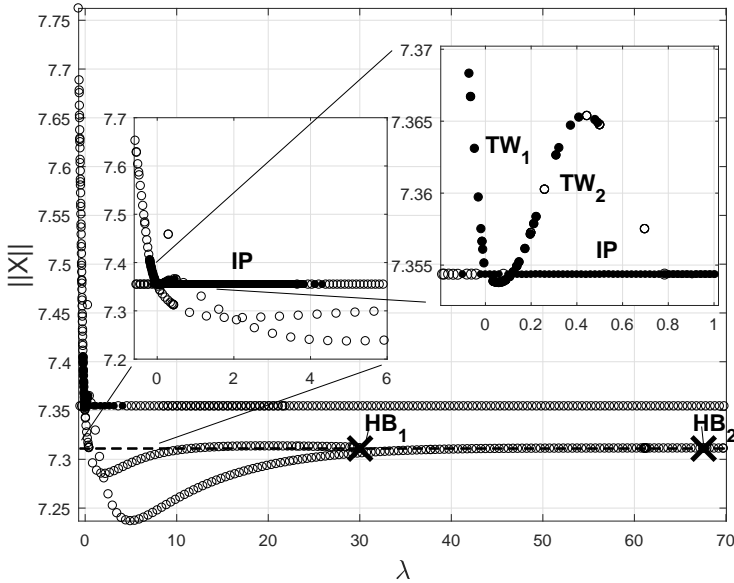


Figure 3.7. Here we see the bifurcation diagram for the governing equations of a Network with three unidirectionally coupled Colpitts oscillators. made using AUTO and MATLAB. We plot the norm of the system vs the coupling strength parameter λ .

A single, unstable equilibrium was calculated for the system, $\|X_e\| = 7.311$. The diagram, Fig. 3.7, shows a line of orbits parallel to the equilibrium. This limit cycle branch contains IP pattern solutions with symmetry $(\mathbb{Z}_3, \mathbb{Z}_3)$. Unlike the TW pattern which emerges from Hopf bifurcations, the existence of IP solutions is independent of λ . Stable, IP periodic solutions are found in the range $0 < \lambda < 4.2$. There are no stable IP limit cycles for values $\lambda < 0$. Two Hopf bifurcations, HB_1 and HB_2 , were found along the equilibrium at values $\lambda_{HB_1} = 30.03$ and $\lambda_{HB_2} = 67.56$. These Hopf bifurcations are characterized by the real part of a complex conjugate pair of eigenvalues switching from negative to positive [19]. Each bifurcation point leads to branches of collective oscillation patterns in the network. Going from left to right, the first Hopf bifurcation found at $\lambda_{HB_1} = 30.03$ leads to a branch of unstable TW type orbits for $0 < \lambda < 30.03$ and stable TW orbits for $-0.2 < \lambda < 0$. The TW

solutions that emerges for HB_1 have $(\mathbb{Z}_3, 1)$ symmetry and are generated by $\gamma_1 = \langle \frac{T}{3} \rangle$. They have the pattern:

$$TW_1 := X(t) = \left(x_1(t), x_1\left(t + \frac{T}{3}\right), x_1\left(t + \frac{2T}{3}\right) \right).$$

The second Hopf bifurcation, $\lambda_{HB_2} = 67.56$, similarly leads to unstable TW orbits in the interval $.55 < \lambda < 67.57$ and stable TW solutions at $0 < \lambda < .55$. This TW corresponds to the same isotropy subgroup as TW_1 but is generated by $\gamma_2 = \langle \frac{2T}{3} \rangle$. The pattern is of the form:

$$TW_2 = \left(x(t), x\left(t + \frac{2T}{3}\right), x\left(t + \frac{T}{3}\right) \right).$$

The interval containing stable TW_1 solutions does not display other types of stable patterns. This is the ideal scenario because even though selecting initial conditions is trivial during simulations, initial conditions cannot be chosen in practice. Contrary to the aforementioned interval, both IP and TW_2 stable orbits are seen in $0 < \lambda < .55$. This is not a practical scenario as the type of solution that emerges is dependent on initial conditions and basins of attraction. We approximate the basins of attraction in the next section.

In order to understand the regions of existence of various solutions, we extend the numerical bifurcation analysis to trace the positions of Hopf bifurcations as functions of both coupling strength, λ , and resistance, R_L . The other parameters are held fixed. Once the Hopf bifurcation locus are drawn, we classify on which side of the Hopf locus its respective solution exists. Figure 3.8 shows the two-parameter bifurcation diagram for coupling strength, λ , and resistance, R_L .

Figure 3.8 shows that there are no TW solutions for regions where the parameters R_L and λ are too large. From Fig. 3.7, an IP solution branch exists independent of λ and is present on both sides of the Hopf locus.

The case $N = 4$ displays the same qualitative solutions as the case $N = 3$. However, a pattern emerges that is unique to even N oscillators. In this solution, called the standing wave (SW) pattern, we see every other oscillator synchronize into the same wave and then shift out of phase by $T/2$ as seen in Section 3.2. This rotation can be seen as being generated by $\gamma^3 = \langle T/2 \rangle$, and the pattern is as follows:

$$SW := \left(x(t), x\left(t + \frac{T}{2}\right), x(t), x\left(t + \frac{T}{2}\right) \right).$$

This pattern also leads to a scaling error of $1/\sqrt{N}$ similar to what would be seen for IP solutions or averaged oscillators [5]. The bifurcation diagram as a function of λ for the case $N = 4$ is seen in Fig. 3.9.

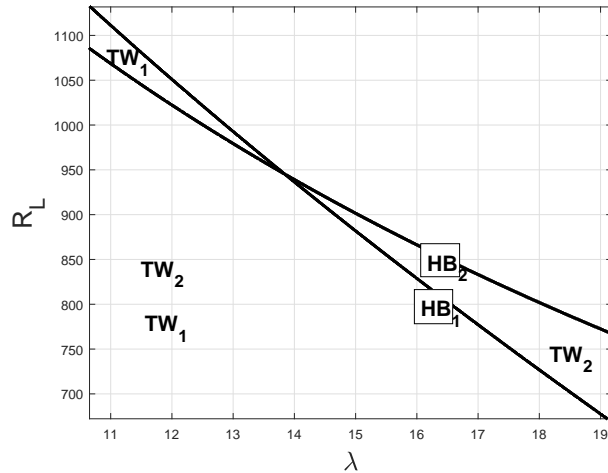


Figure 3.8. Two-parameter bifurcation performed on the system with resistance vs coupling strength axis. The lines represent Hopf bifurcation locus. Both type of TW solutions can be seen on the left side of the Hopf bifurcation locus. Their solution stability depends on the coupling strength value and initial conditions.

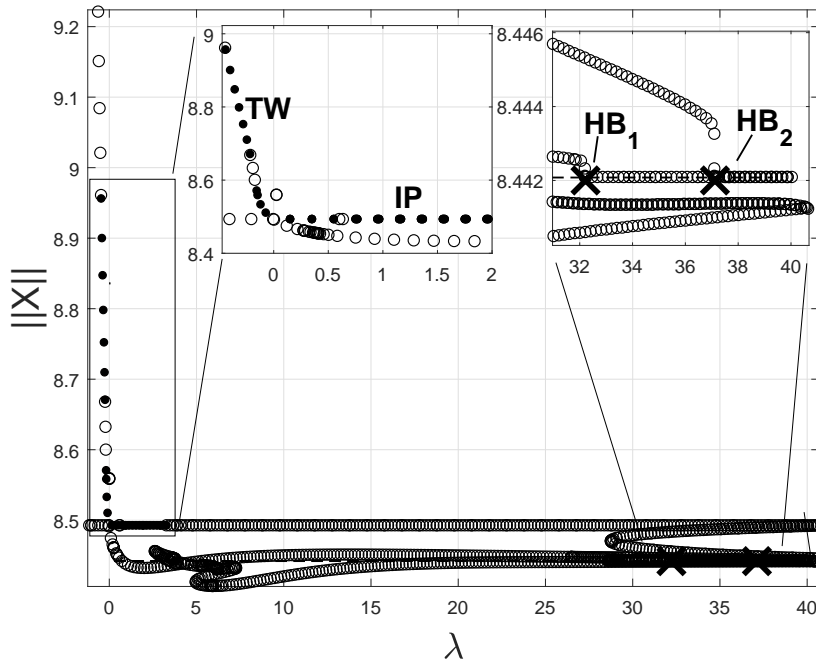


Figure 3.9. Bifurcation diagram for the case of four coupled Colpitts oscillators plotted in norm vs coupling strength axis.

Similar to the case $N = 3$, a single, unstable equilibrium point was found at $\|X\| = 8.442$. A line of IP solutions runs parallel to the equilibrium with isotropy subgroup $(\mathbb{Z}_4, \mathbb{Z}_4)$. Like the case $N = 3$, this implies that the existence of IP solutions is independent of coupling strength

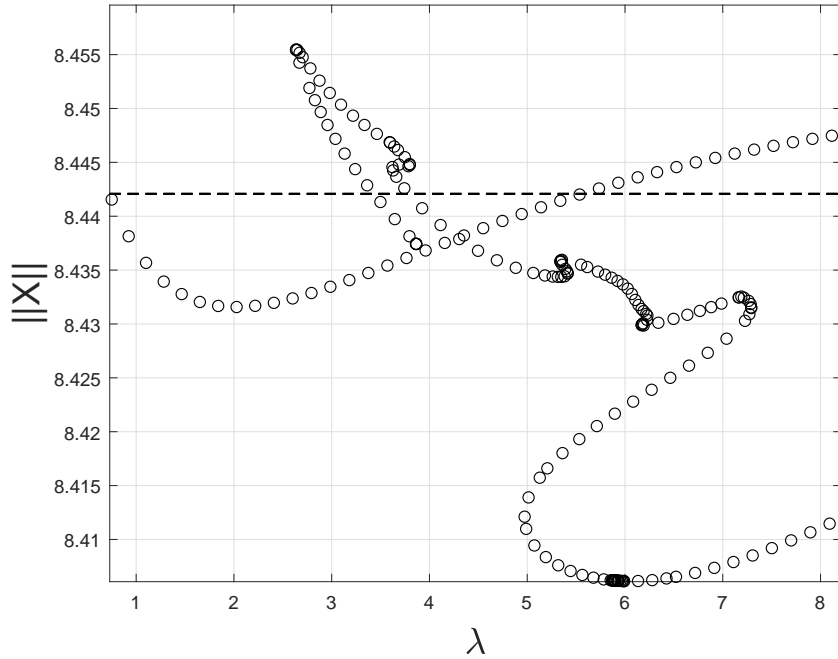


Figure 3.10. This is a magnification of Fig. 3.9 for $0 < \|X\| < 8.5$ where HB_1 branches off into unstable SW type orbits. Note the complexity and abundance of limit points.

variations. The branch of IP solutions is stable in the domain $0 < \lambda < 3.3$. Hopf bifurcations were calculated at the values $\lambda_{HB_1} = 32.22$ and $\lambda_{HB_2} = 37.12$. HB_1 leads to a branch of unstable SW orbits with group symmetry $(\mathbb{Z}_4, \mathbb{Z}_2)$. The branch grows in complexity as λ decreases away from $\lambda_{HB_1} = 32.22$. Fig. 3.10 shows a magnification of that branch. *AUTO* numerical continuation was not able to calculate stable SW solutions by branching off of HB_1 due to the high number of limit and branching points that complicate numerical continuation. Stable and unstable TW solutions emerge from HB_2 with isotropy subgroup $(\mathbb{Z}_4, \mathbb{I})$. The domain for the TW stable orbits appears in negative λ values around $-0.6 < \lambda < 0$.

The Hopf bifurcation locus shown in our two-parameter bifurcation diagram, Fig. 3.11, follows similar trends to the case $N = 3$. They intersect at a single point and imply that TW solutions for overly large values of R_L and λ do not exist. The most noticeable difference is that one of the Hopf locus in $N = 4$ corresponds to the reflectional symmetry pattern, SW.

The case $N = 5$ introduces new TW variants induced from the increase in oscillators. Four different Hopf bifurcations were found at the values $\lambda_{HB_1} = 28.67$, $\lambda_{HB_2} = 45.91$, $\lambda_{HB_3} = 46.73$, and $\lambda_{HB_4} = 205.3$. Each Hopf point corresponds to a different type of TW pattern: TW_1 , TW_2 , TW_3 , TW_4 respectively. TW_3 and TW_4 display the standard TW with group symmetry $(\mathbb{Z}_5, \mathbb{I})$ generated by $\gamma_4 = \langle \frac{4T}{5} \rangle$ and $\gamma_1 = \langle \frac{T}{5} \rangle$ respectively. The patterns are as follows:

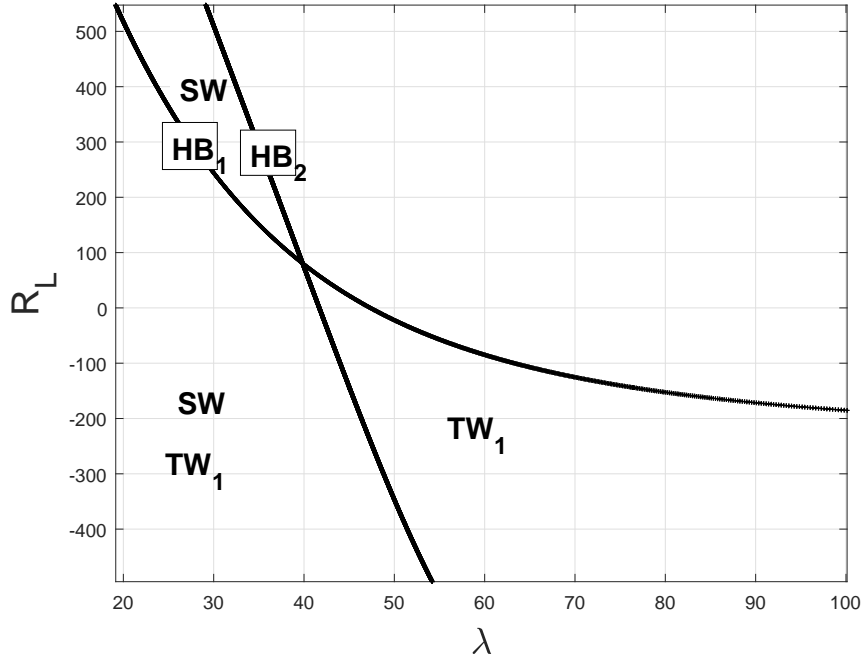


Figure 3.11. Two-parameter bifurcation diagram of resistance vs coupling strength. The lines represent Hopf bifurcation locus. As with the previous case, TW and SW type solutions exist to the left of the Hopf bifurcation locus, and the stability of such orbits depend on initial conditions and coupling strength.

$$\begin{aligned} TW_3 := X(t) &= \left(x_1(t), x_1\left(t + \frac{4T}{5}\right), x_1\left(t + \frac{3T}{5}\right), x_1\left(t + \frac{2T}{5}\right), x_1\left(t + \frac{T}{5}\right) \right); \\ TW_4 := X(t) &= \left(x_1(t), x_1\left(t + \frac{T}{5}\right), x_1\left(t + \frac{2T}{5}\right), x_1\left(t + \frac{3T}{5}\right), x_1\left(t + \frac{4T}{5}\right) \right). \end{aligned} \quad (3.14)$$

TW_1 and TW_2 belong to the same isotropy subgroup as TW_3 and TW_4 ; however, they are generated by $\gamma^2 = \langle \frac{2T}{5} \rangle$ and $\gamma^3 = \langle \frac{3T}{5} \rangle$ respectively. The collective pattern is:

$$\begin{aligned} TW_1 := X(t) &= \left(x_1(t), x_1\left(t + \frac{2T}{5}\right), x_1\left(t + \frac{4T}{5}\right), x_1\left(t + \frac{T}{5}\right), x_1\left(t + \frac{3T}{5}\right) \right); \\ TW_2 := X(t) &= \left(x_1(t), x_1\left(t + \frac{3T}{5}\right), x_1\left(t + \frac{T}{5}\right), x_1\left(t + \frac{4T}{5}\right), x_1\left(t + \frac{2T}{5}\right) \right). \end{aligned} \quad (3.15)$$

Collectively, stable variants of the TW pattern exist in the domain $-0.21 < \lambda < 1.1$. From Fig. 3.12, positive values of this range contain an overlap of three different TW stable orbits. This λ range is shared by stable IP solutions seen in the straight line running parallel to the equilibrium point. Like the case $N = 3$, the one-parameter bifurcation diagram shows a negative region close to $\lambda = 0$ containing exclusively the TW_1 pattern. The observation that

ensembles with an odd number of CCO have small, negative regions of exclusive stable TW behavior is later explored to measure phase drift scaling.

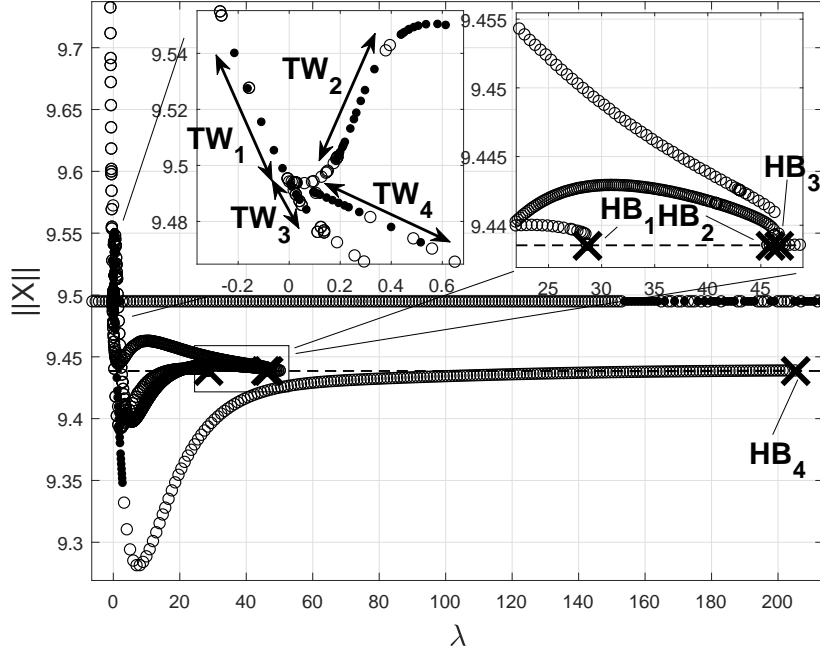


Figure 3.12. Bifurcation diagram shown in norm of system vs coupling strength plot for a NCCOs composed of five oscillators. All four Hopf bifurcations led to their unique set of stable TW orbits with different behavior.

The two-parameter bifurcation diagram seen in Fig. 3.13 shows a noticeably more complex diagram. In contrast to the previous cases, the system with five oscillators goes through four Hopf bifurcations. The locus of these Hopf bifurcations have the same pseudo-downward concavity that the locus for cases $N = 3$ and 4 display. However, the number of distinct solution regions increases, and each region has its unique combination of different possible TW patterns. The two-parameter diagram is consistent with the fact that there do not exist TW solutions for big values of the (λ, R_L) plane.

For $N = 6$, we encounter all the previously seen solution types but now have two variations of the SW as seen in Section 3.2. The first type of SW can be generated by either $\gamma^2 = \langle \frac{T}{3} \rangle$ or $\gamma^4 = \langle \frac{2T}{3} \rangle$ and has group symmetry $(\mathbb{Z}_6, \mathbb{Z}_3)$. We label the two corresponding solutions as $SW_{1,1}$ or $SW_{1,2}$ which have the following patterns:

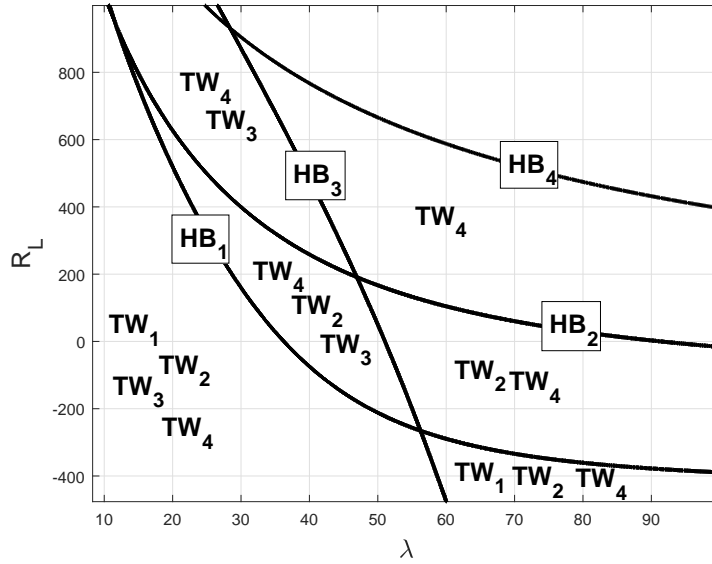


Figure 3.13. Two-parameter bifurcation diagram of resistance vs coupling strength for $N = 5$ oscillators. The lines represent Hopf Bifurcations. These traveling wave solutions exist only to the left side of their respective Hopf locus. Stability of these TW depend on initial conditions and coupling strength.

$$SW_{1,1} := X(t) = \left(x_1(t), x_1\left(t + \frac{T}{3}\right), x_1\left(t + \frac{2T}{3}\right), x_1(t), x_1\left(t + \frac{T}{3}\right), x_1\left(t + \frac{2T}{3}\right) \right);$$

$$SW_{1,2} := X(t) = \left(x_1(t), x_1\left(t + \frac{2T}{3}\right), x_1\left(t + \frac{T}{3}\right), x_1(t), x_1\left(t + \frac{2T}{3}\right), x_1\left(t + \frac{T}{3}\right) \right).$$

The second type of SW seen in Section 3.2 is labeled as SW_2 which belongs to a different isotropy subgroup than SW_1 , $(\mathbb{Z}_6, \mathbb{Z}_2)$. It is generated by $\gamma^3 = \langle \frac{T}{2} \rangle$, and has the pattern:

$$SW_2 := X(t) = \left(x_1(t), x_1\left(t + \frac{T}{2}\right), x_1(t), x_1\left(t + \frac{T}{2}\right), x_1(t), x_1\left(t + \frac{T}{2}\right) \right).$$

Figure 3.14 shows five Hopf bifurcations found at the values $\lambda_{HB_1} = 30.3$, $\lambda_{HB_2} = 32.22$, $\lambda_{HB_3} = 57.78$, $\lambda_{HB_4} = 67.56$, and $\lambda_{HB_5} = 287.7$. HB_1 , branches off into unstable orbits with the first type of standing wave behavior, $SW_{1,1}$. HB_2 branches off into unstable SW solutions of the second type, SW_2 . HB_3 leads to a branch of unstable TW_3 orbits generated by $\gamma^5 = \langle \frac{5T}{6} \rangle$ that belong to the isotropy subgroup $(\mathbb{Z}_6, \mathbb{1})$, and HB_4 branches off into unstable and stable orbits with $SW_{1,2}$ pattern. Standard TW patterns, TW_5 , generated by $\gamma^1 = \langle \frac{T}{5} \rangle$ emerge from HB_5 . The branch of periodic orbits running parallel to the equilibrium seen in the Fig. 3.14 and 3.15 has group symmetry $(\mathbb{Z}_6, \mathbb{Z}_6)$ and correspond to IP solutions. The non-IP stable orbits of all previous bifurcation diagrams are qualitatively similar and

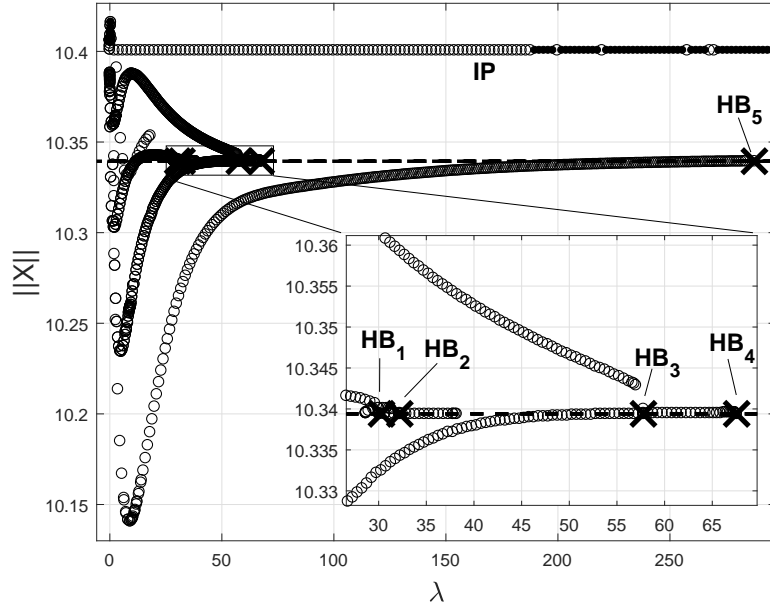


Figure 3.14. This is the bifurcation diagram for the case $N = 6$ plotted in a norm vs coupling strength axis. Three of the five Hopf bifurcations lead to large branches of stable and unstable orbits, but HB_2 has a shorter branch that AUTO was not able to expand. We show only the branches that AUTO produced.

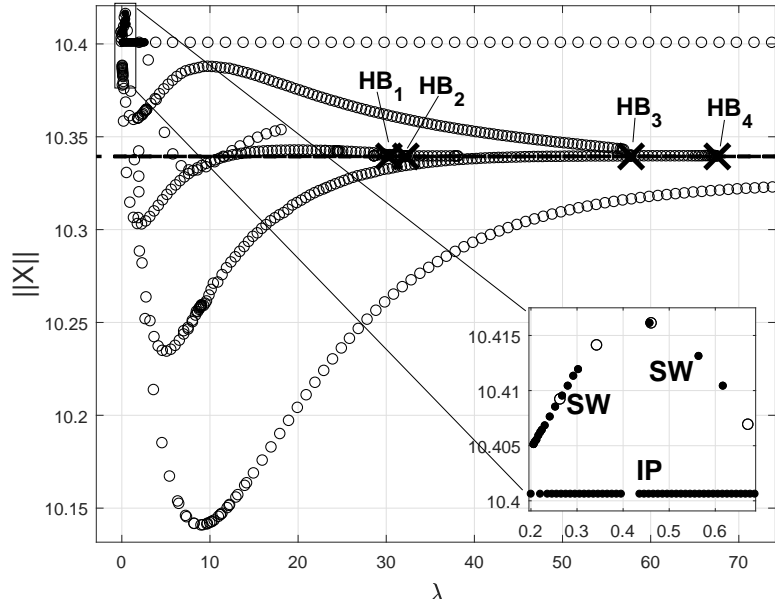


Figure 3.15. Fig. (3.14) expanded about Hopf bifurcations HB_1 to HB_4 . The stable SW can be seen close to $\lambda = 0$.

correspond to TW solutions with group symmetry $(\mathbb{Z}_N, \mathbb{1})$, but in the case $N = 6$, the stable orbits belong to SW solutions. They are found in a small, positive λ range. The range that this pocket of SW solutions occupies is shared by stable IP orbits.

As is shown in Section 3.2, a consequence of having a higher number of coupled oscillators is an increase in possible solution branches guaranteed by the EHT. This result can be observed in Fig. 3.16 showing the two-parameter bifurcation diagram with varying λ and R_L . This case remains consistent with the previous by displaying IP solutions independent of λ variations. Variations of rotating wave solutions exist for values below the Hopf locus while the only solutions for values above the the locus are IP solutions.

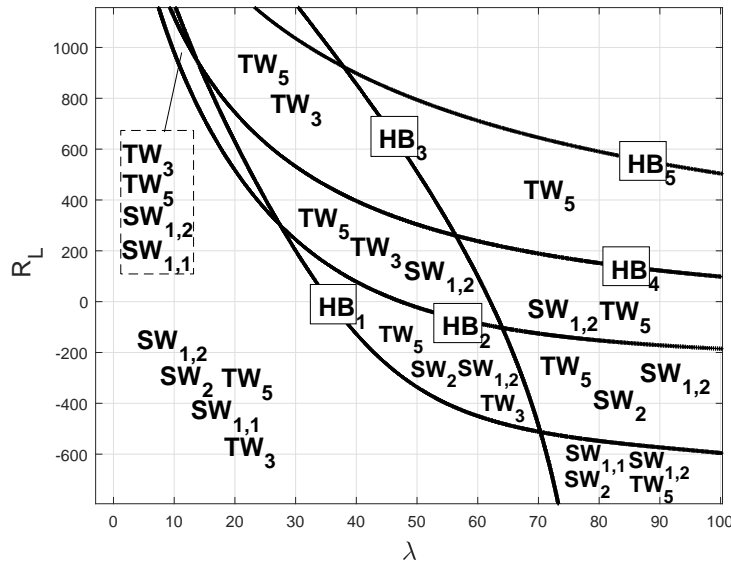


Figure 3.16. Two-parameter bifurcation diagram of R_L vs λ . The lines represent Hopf bifurcation locus. The stability of the orbits depend on initial condition and coupling strength.

The numerical bifurcation analysis seen in this section shows the existence of many solution types predicted by the (\mathbb{Z}_N, S^1) symmetry.

3.4 BASINS OF ATTRACTION

As mentioned in the previous section, at a specific λ there might be multiple solutions, unless a solution is globally asymptotically stable. Depending on initial conditions, a single λ value can be associated with different solution types. This poses a problem as it makes the one-parameter bifurcation diagrams with varying λ insufficient for finding regions where the system exhibits dominant TW behavior. Thus, we create a probability distribution function plot for varying values of λ . This gives us insight into the size of each solution's basin of

attraction and allows us to see the probability of encountering said solutions per λ value. The probability distribution was calculated by performing 100 system simulations per λ value ten times. We integrate with random uniformly distributed initial conditions, \bar{r} , with elements $r_k \in [0, 5]$ for $k = 1, 2, \dots, 3N$. The system of ODEs was integrated using a Runge-Kutta 2 integration scheme. Once integrated, the solution was classified as either TW, SW, IP, or QP.

IP solutions are identified by subtracting the solution vectors of individual oscillators. An average of the total difference between solution vectors close to 0, within a tolerance $\epsilon = 1.0e - 14$, indicated IP behavior. TW solutions were identified by using theoretical information about the phase shift seen in systems with \mathbb{Z}_N symmetry. A system of N oscillators displaying TW behavior exhibits a phase shift between oscillators of length T/N . The period, T , of a single oscillator is estimated by identifying all the peaks in the solution. The data of a reference oscillator is then shifted by $T/N, N - 1$ amount of times to simulate the theoretical phase shift. The difference between original solution vectors and the artificial TW data is then calculated. To account for the different TW generated by multiple generators, the difference was computed between the solution vectors and permutations under actions of generators, $\gamma \in \mathbb{Z}_N$, of the artificial data. If a difference between the permuted initial wave and a solution was within tolerance, the solution was classified as having TW behavior. A solution was classified as SW if there was at least one, but less than $N - 1$, difference vectors between solutions within tolerance. These three patterns are the main solutions of interest, so waves that did not fit into the previous categories were classified as Quasi-Periodic (QP) or other. In the following diagrams, filled-in dots indicate IP solutions, empty circles label TW solutions, \times correspond to SW, and asterisks indicate QP or other types of solutions.

Figure 3.17 shows the solution type probability function for the case $N = 3$. It is readily apparent that the only region where the system has 100% traveling wave solutions is in a small interval with a range of approximately $-0.19 \leq \lambda \leq -0.03$. It is possible that the range extends to include negative λ values arbitrarily close to 0, but coupling strength values of that magnitude are difficult to classify as they require large transient times. Shortly after λ passes 0 into the positive regime, combinations of IP solutions along with small amounts of TW solutions emerge. This is consistent with our one-parameter analysis for this range. Based off of the solution distribution for small positive λ , IP patterns have a larger basin of attraction than the TW solution. The size of the basins of attraction of IP solutions starts to decrease as λ increases, and the basin of TW solutions increases. This trend continues until TW orbits lose stability and the basin of attraction is populated by QP solutions. As we increase λ , we eventually reach a point where the only type of stable orbit solutions possible are QP solutions.

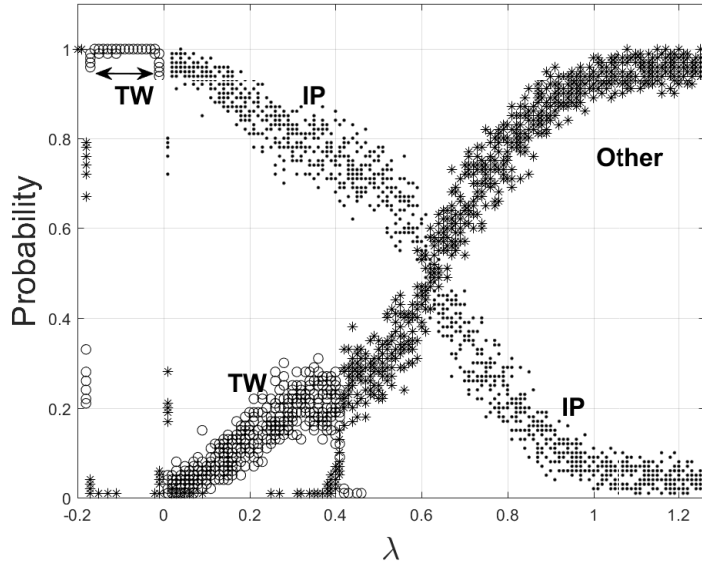


Figure 3.17. Probability distribution of solution types for different coupling strength values for the case of three coupled Colpitts oscillators.

Fig. 3.18 shows the same qualitative behavior between the case $N = 4$ and $N = 3$ for positive values of λ . The basin of attraction for IP solutions is dominant for positive λ close to 0 with small probability of TW solutions. As we go larger in the positive domain, we lose all types of solutions except those with QP behavior. The most obvious difference between the positive regime of $N = 3$ and $N = 4$ is the emergence of a minute basin of attraction containing SW solutions with $(\mathbb{Z}_4, \mathbb{Z}_2)$ symmetry for small positive coupling values. The basin of attraction corresponding to the SW pattern increases significantly for negative values of λ . Although our one-parameter analysis resulted in solely stable TW solutions for negative λ close to 0, the probability density diagram shows that that region contains higher probability of SW solutions. This suggests a large, dominant basin of attraction for SW solutions that was not captured by our one-parameter bifurcation diagram. There are no values of λ for which we have exclusively TW solutions. This helps validate the observation that having an even number of oscillators is not optimal for application purposes [5]. The probability distribution results for $N = 5$ seen in the Fig. 3.19 are qualitatively the same as those in $N = 3$ for all observed λ values. Most importantly, there exists a range of λ where we have a 100% probability of encountering TW solutions. The TW pattern seen for these values is generated by the group element $\gamma^2 = \langle \frac{2T}{5} \rangle$ and has group symmetry $(\mathbb{Z}_5, \mathbb{1})$. Although not the standard TW configuration generated by the group element $\gamma^1 = \langle \frac{T}{5} \rangle$, this pattern also results in the desired scaling of $1/N$. The solution type probability plot for cases

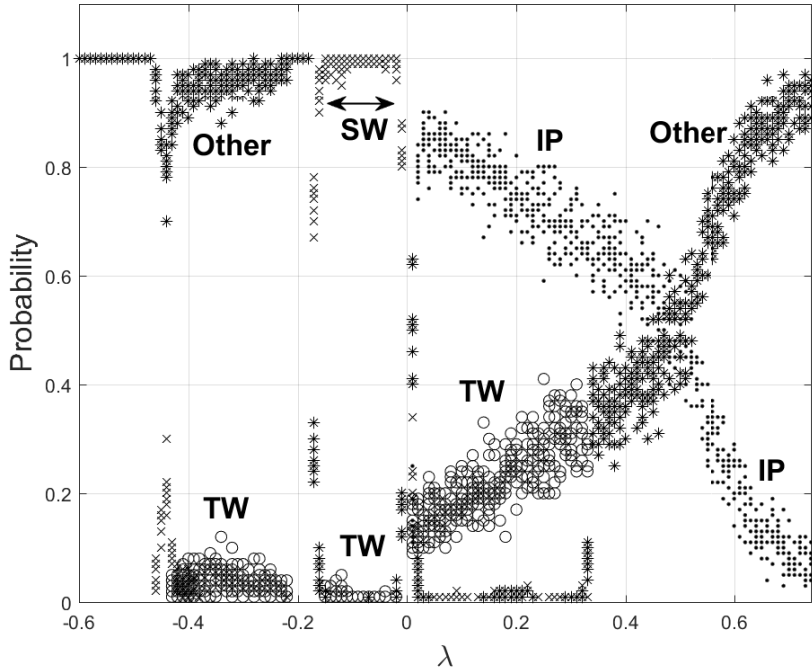


Figure 3.18. Probability density for different solution types of the case of four coupled Colpitts oscillators. We can see that the negative regime of the plot displays richer dynamics than that of case $N = 3$.

$N = 3$ and $N = 5$ further the argument that the envisioned precision timing device should consist of only an odd number of oscillators [5].

This probability density function diagram for $N = 6$, Fig. 3.20, shares similar behavior to that seen in the case $N = 4$. Fig. 3.20 shows the SW pattern basin of attraction as dominant for small negative λ similar to the case $N = 4$. There was no distinction made when classifying different types of SW solutions such as those with group symmetry $(\mathbb{Z}_6, \mathbb{Z}_2)$ and $(\mathbb{Z}_6, \mathbb{Z}_3)$.

However, there does not exist a small basin of TW solutions for this region. This is consistent with our one-parameter bifurcation diagram. TW solutions were found for the positive regime which did not appear as stable TW orbits in Fig. 3.16. There does not appear to be any regions where the TW solution is dominant.

The solution type probability density functions described in this section coupled with our bifurcation diagrams provide us with insight when choosing coupling strength values that guarantee TW solutions regardless of initial conditions. As observed in this section, NCCOs with an odd number of oscillators potentially have small negative λ regions where the TW solutions are dominant. In the next section, we exploit this observation to calculate the phase drift and validate the phase drift scaling of $1/N$ that stems from the TW pattern.

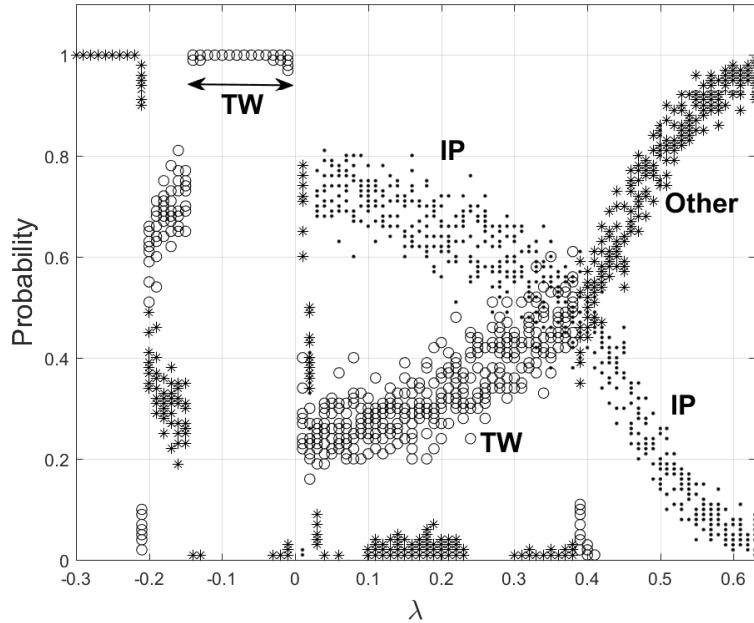


Figure 3.19. Probability density for different solution types for the case of five CCOs. The behavior seen here is similar to the case $N = 3$.

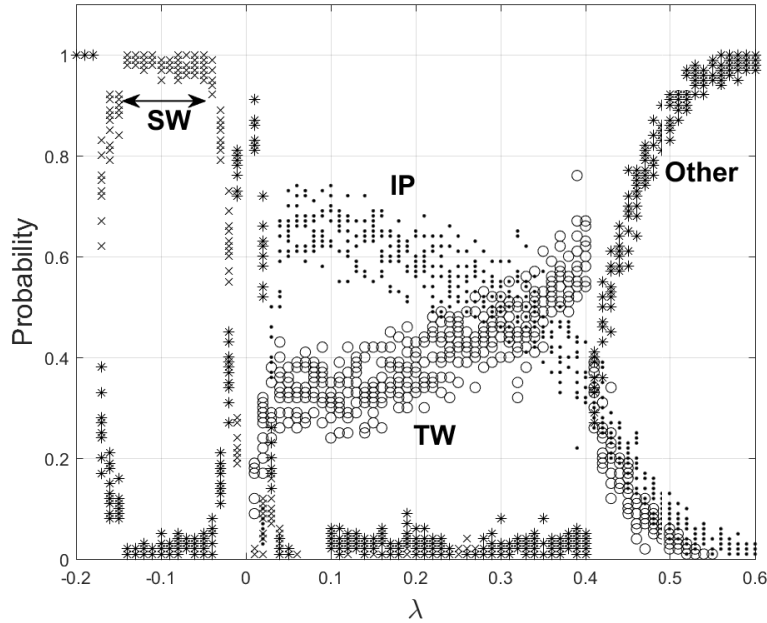


Figure 3.20. Probability density plot for different solution types of the case with six coupled Colpitts oscillators. In this scenario, we do not differentiate between the two different type of SW solutions. Instead, we classify them both as SW. It is apparent that the dynamics become more complex, and numerical classification becomes more difficult due to the higher number of oscillators and increase in the transient time needed to fully converge to a solution.

3.5 PHASE-DRIFT CALCULATIONS

The envisioned precision timing device is built upon the concept that TW solutions will give rise to a decrease in phase drift error in the form of $1/N$. We have identified coupling strength parameters where TW is the dominant solution. With that information in hand, we strive to calculate the phase drift error and identify coupling strength value regions for which phase error scaling has the form $1/N$.

Simplifying assumptions were made when analyzing and modeling the Colpitts oscillator. It is assumed that all oscillators are identical and we neglect material and manufacturing imperfections that lead to noise and phase drift error. The phase drift analysis will be done numerically by comparing numerical solutions of our network of CCO with banded noise and solutions of the system without noise. The equations are cast into a stochastic model that includes colored noise to simulate electronic component fluctuations. The colored noise is introduced as an Ornstein-Uhlenbeck process and has non zero correlation time, τ_c , which makes this type of noise a more faithful representation of the noise in the circuit than Gaussian noise [17]. We ensure that the noise does not drive the signal of the oscillators by setting $\tau_c \gg \tau_f$ where τ_f is the time constant of the oscillator [5, 10, 17]. The noise, ξ_n , is Gaussian band-limited with 0 mean and variance of $\sigma^2 = 1$ [10]. Colored noise, $\eta(t)$, is introduced in the system by rewriting our system of equations in Langevin form:

$$\begin{aligned} \frac{dX_n}{dt} &= F(X) + \eta_n \\ \frac{d\eta_n}{dt} &= -\frac{\eta_n}{\tau_c} + \frac{\sqrt{2D}}{\tau_c} \xi_n(t). \end{aligned} \quad (3.16)$$

Each noise component is characterized by $\langle \eta_i \rangle = 0$ and $\langle \eta_i(t)\eta_j(s) \rangle = \frac{1}{2\tau_c}e^{-|t-s|/\tau_c}$ [1, 17]. As $\tau_c \rightarrow 0$, the noise loses its non zero correlation and Gaussian noise is recovered [1, 17]. The system is integrated using the stochastic differential equations solver, the Euler-Maruyama scheme. The solution to the system with noise can be seen in Fig. 3.21. The value D is chosen through experimentation and analysis of the Power Spectral Density (PSD) to ensure the noise does not drown out the signal. After a transient time, the periods of oscillations are calculated per individual oscillators. The periods of oscillations are obtained by calculating the zero-crossings of the solution. The zero-crossings of the data are estimated using 3-point quadratic interpolation. We calculate 600 periods of each oscillator solution with noise, $\tilde{P}_k = [p_{k,1}, p_{k,2}, \dots, p_{k,600}]$, and the same amount of periods of each oscillator without noise, $P_k = [p_{k,1}, p_{k,2}, \dots, p_{k,600}]$. We then calculate

$$PE_k = |\tilde{P}_k - P_k|$$

$$PE_{Average} = \frac{1}{N} \sum_{k=1}^N PE_k.$$

Since we are dealing with very small phase drift values, we opt for calculating the absolute mean deviations instead of the standard deviation:

$$\text{Phase Drift} = \frac{1}{600} \sum_{i=1}^{600} |PE_{Average}^i - \overline{PE_{Average}}|.$$

This leaves us with phase drift information of the system. We repeat this process with 20 samples and average out the results per every N case. Figure 3.22 shows the phase drift calculations for the uncoupled case.

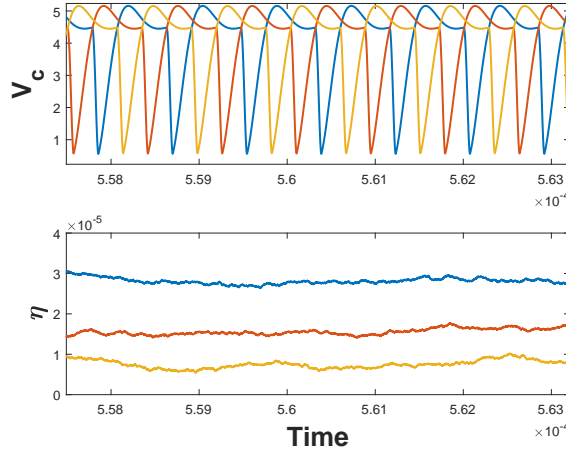


Figure 3.21. Voltage portion of the solution for the circuit model in Langevin form. The bottom plot, η , shows the colored noise obtained through the Ornstein-Uhlenbeck process. Note the difference in magnitudes between the noise and the actual solution of the system.

Although we have TW solutions for small negative λ , not all coupling strength values in that interval lead to the $1/N$ scaling. To pinpoint the correct parameter value, we iterate through λ and calculate the respective phase drift scaling. This is a computationally intensive calculation as the Euler-Maruyama scheme requires small time steps to converge within a measure of success to the desired solution. We calculate the phase drift of odd cases $N = 2j + 1$ for $j = 1, 2, 3, 4, 5$ and average out 20 iterations per case. The results can be seen in Fig. 3.23. The plot shows the value $\lambda = -0.05$ displays scaling improvement close to that of $1/N$. As we move further into the negative domain, the system undergoes period doubling and even chaotic behavior, thus accounting for the increase in phase drift error. These are tentative

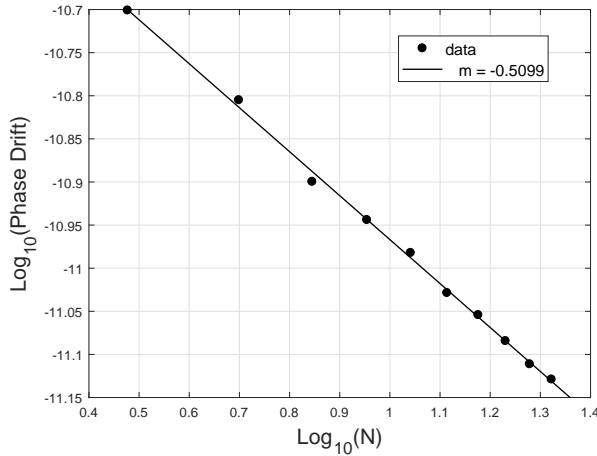


Figure 3.22. Phase drift error calculations for uncoupled oscillators. The phase drift was calculated for 20 samples and averaged for each case of number of oscillators. A least square linear regression line is plotted on the Log of the phase drift vs the Log of the number of oscillators, N . The slope, m , represents the scaling exponent, $1/N^m$. This validates the prediction that uncoupled oscillators have a phase error scaling of $1/\sqrt{N}$

results as a deeper analysis is needed of the Euler-Maruyama's scheme convergence for our system of equations.

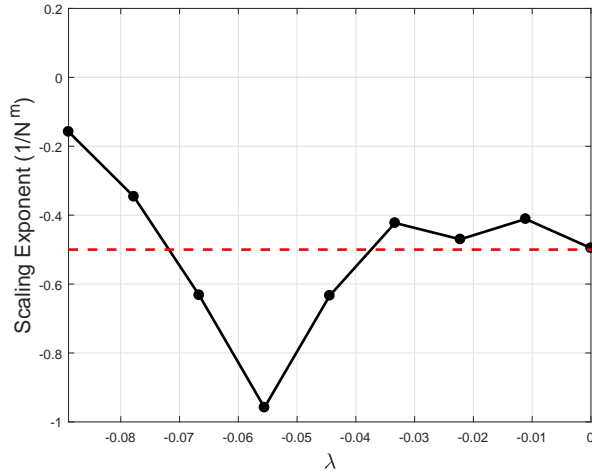


Figure 3.23. Tentative results for phase drift calculations with noise level $D = 1 \times 10^{-13}$ chosen through experimentation. The values of the y-axis display the scaling exponent m which corresponds to scaling $1/N^m$. Iterations through small, negative λ values yielded a small region where we see scaling improvement approaching $1/N$.

Note that although the entire range seen in Fig. 3.23 exhibits TW type solutions, values of λ close to 0 display slightly worse scaling than that of that of the uncoupled case. This is

consistent with the scaling near $\lambda = 0$ observed in the work done on the network of coupled crystal oscillators.

CHAPTER 4

NETWORK WITH IDEAL MODEL

In this chapter, we study the collective behavior of the NCCO by analyzing the ideal model equations introduced in Section 2.5. These equations are also used to compute the eigenvalues of our system.

4.1 GOVERNING EQUATIONS

The reduced equations, or “Ideal Model”, retain the complexity and governing dynamics of the original Colpitts oscillator equations but presents a set of phenomenological equations that simplify analysis. They allow us to perform eigenvalue calculations and stability analysis of the system. Kirchoff’s voltage law is used to couple the oscillators along the first equation, x_{i1} . This mirrors the coupling of the first capacitor, C_1 , seen in the circuit equations. We have the following “Ideal Model” for Networks of CCOs:

$$\begin{aligned} \frac{dx_{i1}}{dt} &= \frac{g}{Q(1-\kappa)} \left[-\left(e^{-x_{i2}} - 1\right) + x_{i3} \right] + \lambda (x_{i+1,1} - x_{i1}) \\ \frac{dx_{i2}}{dt} &= \frac{g}{Q-\kappa} x_{i3} \\ \frac{dx_{i3}}{dt} &= -\frac{Qk(1-\kappa)}{g*} (x_{i1} + x_{i2}) - \frac{1}{Q} x_{i3}. \end{aligned} . \quad (4.1)$$

In the next section, we calculate the eigenvalues of case $N = 3$ for our system (4.1).

4.2 ASYMPTOTIC APPROXIMATION OF EIGENVALUES

In this section, we exploit dimensionality reduction of our system seen in Eq. (4.1), to compute the eigenvalues and, as a consequence, the values of λ that lead to Hopf bifurcations. The case $N = 3$ is given as an example. Let

$$X_j = [x_{j,1}, x_{j,2}, x_{j,3}]^T, \quad (4.2)$$

such that

$$\begin{aligned} \dot{X}_1 &= f(X_1; \lambda) + C(\lambda)(X_2 - X_1) \\ \dot{X}_2 &= f(X_2; \lambda) + C(\lambda)(X_3 - X_2) \\ \dot{X}_3 &= f(X_3; \lambda) + C(\lambda)(X_1 - X_3), \end{aligned} \quad (4.3)$$

where $f(X_1)$ is the matrix representation of Eq. (2.7)

$$f(X_j) = \begin{bmatrix} \frac{g}{Q(1-\kappa)} [-(e^{-x_{j,2}} - 1) + x_{j,3}] \\ \frac{g}{Q\kappa} x_{j,3} \\ -\frac{Q\kappa(1-\kappa)}{g} (x_{j,1} + x_{j,2}) - \frac{1}{Q} x_{j,3} \end{bmatrix} \quad (4.4)$$

and $C(\lambda)$ is the coupling matrix

$$C(\lambda) = \lambda \begin{bmatrix} 1 & 0 & 0 \\ 0 & 0 & 0 \\ 0 & 0 & 0 \end{bmatrix}. \quad (4.5)$$

We linearize this system as

$$L = \begin{bmatrix} A & B & 0 \\ 0 & A & B \\ B & 0 & A \end{bmatrix} \quad (4.6)$$

for $A = (df)_{(0,0)} - C(\lambda)$ and $B = C(\lambda)$ where $(df)_{(0,0)}$ is the Jacobian matrix of a single Colpitts cell shown in Eq. (2.8). The subgroups of \mathbb{Z}_3 are used to decompose our system's Jacobian, L , in block diagonal form via the isotypic decomposition of the phase space \mathbb{R}^9 . The representation of \mathbb{Z}_3 on \mathbb{R}^9 is broken into real irreducible representations each corresponding to an isotropy subgroup [11]. Let $\zeta = \exp(2\pi i/3)$ and $v_j = [v, \zeta^j v, \zeta^{2j} v]^T$ for $j = 0, 1, 2$ be three vectors in \mathbb{C} for some $v \in \mathbb{R}$. The vectors v_j form the basis for \mathbb{C}^3 :

$$\mathbb{C}^3 = \mathbf{V}_0 \oplus \mathbf{V}_1 \oplus \mathbf{V}_2. \quad (4.7)$$

The governing equations for each colpitts oscillator have a phase space of dimension three. Thus, we consider the basis vectors $\{e_1, e_2, e_3\}$ of \mathbb{R}^3 and define

$$v_{jk} = [e_k, \zeta^j e_k, \zeta^{2j} e_k]^T, \quad (4.8)$$

for $k = 1, 2, 3$. This set of vectors form a basis for the complexified phase space

$$\mathbb{C}^9 = \mathbf{V}_0^3 \oplus \mathbf{V}_1^3 \oplus \mathbf{V}_2^3. \quad (4.9)$$

Let \mathcal{I}_{jk} and \mathcal{R}_{jk} denote the imaginary and real part, respectively, of the vector v_{jk} . We define the transformation matrix

$$P = [v_{01}, v_{02}, v_{03}, \mathcal{I}_{11}, \mathcal{I}_{12}, \mathcal{I}_{13}, \mathcal{R}_{11}, \mathcal{R}_{12}, \mathcal{R}_{13}]. \quad (4.10)$$

Under transformation $V = UP$, the linearization of the system can be transformed as $\mathcal{L} = P^{-1}LP$ which is the block diagonalized matrix

$$\mathcal{L} = \left(\begin{array}{c|c} (df)_{(0,0)} & 0 \\ \hline 0 & M(2\pi/3) \end{array} \right),$$

for

$$M(2\pi/3) = \mathbf{I}_2 \otimes A + \mathbf{R}(2\pi/3) \otimes B \quad (4.11)$$

where \otimes denotes Kronecker product and $\mathbf{R}(2\pi/3)$ represents the matrix of rotations by $\theta = 2\pi/3$,

$$\mathbf{R}(2\pi/3) = \begin{bmatrix} \cos(2\pi/3) & -\sin(2\pi/3) \\ \sin(2\pi/3) & \cos(2\pi/3) \end{bmatrix}. \quad (4.12)$$

The eigenvalues of \mathcal{L} are given by the union of the eigenvalues of matrices $(df)_{(0,0)}$ and $M(2\pi/3)$. Section 2.5 shows calculations of the eigenvalues for $(df)_{(0,0)}$. This block matrix corresponds to the trivial representation, or symmetry group $(\mathbb{Z}_3, \mathbb{Z}_3)$ and as seen in Section 2.5, the eigenvalues are invariant under changes in λ . Thus, solutions with IP pattern exist for all values of λ as observed in the system's numerical analysis. The group $(\mathbb{Z}_3, \mathbb{1})$ is represented by the block matrix $M(2\pi/3)$. The block matrix corresponding to the TW pattern has the form

$$M(2\pi/3) = \left(\begin{array}{c|c} D & -E \\ \hline E & D \end{array} \right)$$

for $D = A + \cos(2\pi/3)B$ and $E = \sin(2\pi/3)B$. The eigenvalues of the block matrix can be calculated as $eig(M(2\pi/3)) = eig(D + iE) \cup eig(D - iE)$ where

$$\begin{aligned} \mathcal{M}_1 &= D - iE = ((df)_{(0,0)} - C(\lambda)) + \zeta C(\lambda) \\ \mathcal{M}_2 &= D + iE = ((df)_{(0,0)} - C(\lambda)) + \zeta^2 C(\lambda). \end{aligned}$$

By letting

$$\begin{aligned} \mathcal{A}_+ &= (\zeta - 1) = -1 + \cos(2\pi/3) + \sin(2\pi/3)i, \\ \mathcal{A}_- &= (\zeta^2 - 1) = -1 + \cos(2\pi/3) - \sin(2\pi/3)i, \end{aligned} \quad (4.13)$$

we rewrite

$$\begin{aligned} \mathcal{M}_1 &= (df)_{(0,0)} + \mathcal{A}_+ C, \\ \mathcal{M}_2 &= (df)_{(0,0)} + \mathcal{A}_- C. \end{aligned}$$

The eigenvalues of \mathcal{M}_1 are given by the characteristic polynomial

$$|(df)_{(0,0)} + \mathcal{A}_+ C - \sigma I| = \sigma^3 + \left(\frac{1}{Q} - \mathcal{A}_+ \lambda\right) \sigma^2 + \left(1 - \frac{\mathcal{A}_+ \lambda}{Q}\right) \sigma + \mathcal{A}_+ \lambda (\kappa - 1) + \frac{g}{Q} = 0 \quad (4.14)$$

which is equal to Eq. (2.11) when $\lambda = 0$. From Section 2.5, Eq. (2.11) produces eigenvalues

$$\begin{aligned} \sigma_1 &= -\frac{1 + gQ^2}{Q(Q^2 + 1)} \\ \sigma_{2,3} &= \frac{Q}{2(Q^2 + 1)}(g - 1) \pm \left[1 + \frac{1}{2(Q^2 + 1)}(g - 1)\right]i. \end{aligned} \quad (4.15)$$

which are the eigenvalues of the matrix, $(df)_{(0,0)}$. An approximation of the eigenvalues given by Eq. (4.14) is made by letting $\lambda = 0 + \epsilon$, $|\epsilon| \ll 1$:

$$\sigma_{1,2,3}^{\mathcal{M}_1} = \sigma_{1,2,3} + a_{1,2,3}\epsilon. \quad (4.16)$$

By substituting $\sigma_1^{\mathcal{M}_1}$ into Eq. (4.14) and eliminating higher order perturbations, we calculate

$$a_1 = \frac{\mathcal{A}_+(\sigma_1^2 Q + \sigma_1 + Q(1 - \kappa))}{3\sigma_1^2 Q + 2\sigma_1 + Q} \quad (4.17)$$

where a_2 and a_3 can be obtained by substitution of σ_2 or σ_3 respectively. The values $\sigma_{1,2,3}^{\mathcal{M}_1}$ are linear approximations of the eigenvalues of the system $(df)_{(0,0)} + \mathcal{A}_+ C$. The following equation shows the approximation of $\sigma_1^{\mathcal{M}_1}$:

$$\begin{aligned} \sigma_1^{\mathcal{M}_1} &= \left[\frac{(\cos(2\pi/3) - 1) \left(\frac{\beta_1^2}{Q} - \frac{\beta_1}{Q} - Qk + Q \right)}{\left(3\frac{\beta_1^2}{Q} + Q - 2\frac{\beta_1}{Q} \right)} \lambda - \beta_1 \right] \\ &\quad + \left[\frac{\sin(2\pi/3) \left(\frac{\beta_1^2}{Q} - \frac{\beta_1}{Q} - Qk + Q \right)}{\left(3\frac{\beta_1^2}{Q} + Q - 2\frac{\beta_1}{Q} \right)} \lambda \right] i \end{aligned} \quad (4.18)$$

where

$$\beta_1 = \frac{Q^2 g + 1}{Q(Q^2 + 1)}.$$

By following the same procedure used to obtain $\sigma_1^{\mathcal{M}_1}$, we obtain the approximations:

$$\begin{aligned} \sigma_2^{\mathcal{M}_1} &= \left[\left(\frac{\cos(2\pi/3)K - \sin(2\pi/3)P\epsilon R}{R^2 + S^2} + \frac{\sin(2\pi/3)K + \cos(2\pi/3)P\epsilon S}{R^2 + S^2} \right) \lambda + Q\beta_2 \right] \\ &\quad + \left[\left(\frac{\sin(2\pi/3)K + \cos(2\pi/3)PR}{R^2 + S^2} + \frac{\cos(2\pi/3)K - \sin(2\pi/3)PS}{R^2 + S^2} \right) \lambda + 1 + \beta_2 \right] i \end{aligned}$$

and

$$\sigma_3^{\mathcal{M}_1} = \left[\left(\frac{(\cos(2\pi/3) - 1)K + \sin(2\pi/3)PR}{R^2 + S^2} + \frac{\sin(2\pi/3)K + (\cos(2\pi/3) - 1)PS}{R^2 + S^2} \right) \lambda + Q\beta_2 \right] \\ + \left[\left(\frac{\sin(2\pi/3)K - (\cos(2\pi/3) - 1)PR}{R^2 + S^2} - \frac{(\cos(2\pi/3) - 1)K - \sin(2\pi/3)PS}{R^2 + S^2} \right) \lambda - 1 - \beta_2 \right] i$$

where

$$\begin{aligned} \beta_2 &= \frac{g - 1}{2Q^2 + 2}, \\ K &= ((Q^2\beta_2^2 - \beta_2^2 - 2\beta_2 - 1)Q + Q\beta_2 - Qk + Q), \\ P &= ((2Q\beta_2^2 + 2Q\beta_2)Q + 1 + \beta_2), \\ R &= ((3Q^2\beta_2^2 - 3\beta_2^2 - 6\beta_2 - 3)Q + 2Q\beta_2), \\ S &= ((6Q\beta_2^2 + 6Q\beta_2)Q + 2 + 2\beta_2). \end{aligned} \quad (4.19)$$

The matrix \mathcal{M}_1 has three complex eigenvalues. By similarly computing the eigenvalue approximations of \mathcal{M}_2 , we see:

$$\sigma_{1,2,3}^{\mathcal{M}_2} = \overline{\sigma_{1,2,3}^{\mathcal{M}_1}}. \quad (4.20)$$

Thus, the matrix $M(2\pi/3)$ has three pairs of complex conjugate eigenvalues. Hopf bifurcations can be computed through this asymptotic eigenvalue approximation by locating where the real part of the eigenvalues is equal to zero. Using parameter values from Fig. 2.12, the three complex eigenvalue pairs from $M(2\pi/3)$ locate Hopf bifurcations at values $\lambda = \{-2.79683, 0.037566, 0.054431\}$. The numerical bifurcation analysis seen in Section 4.3 provides the numerical Hopf bifurcation λ values for comparison. This method of analysis can be extended to N oscillators. However, as we increase the number of oscillators, the dimensionality of this problem increases, and calculations of these asymptotic approximations become cumbersome. Future work will include analytical eigenvalue calculations by projecting our system onto its center manifold and reducing the dimensionality of the problem. Performing a center manifold reduction about a Hopf bifurcation will simplify the calculations of eigenvalue calculations thus allowing for a generalized stability analysis.

4.3 COMPUTATIONAL BIFURCATION ANALYSIS

The numerical bifurcation analysis of the Ideal Model serves the purpose of validating the results obtained in Section 3.2. Similarly to Section 3.3, we analyze the qualitative behavior of our ensemble by studying one-parameter bifurcation diagrams with the system's norm as a function of λ and two-parameter bifurcation diagrams with varying λ and R_L . Parameters Q , κ and g are chosen and fixed to induce stable, near sinusoidal solutions.

We begin by looking at the one-parameter bifurcation diagram for case of three coupled Colpitts oscillators. The diagram can be seen in Fig. 4.1.

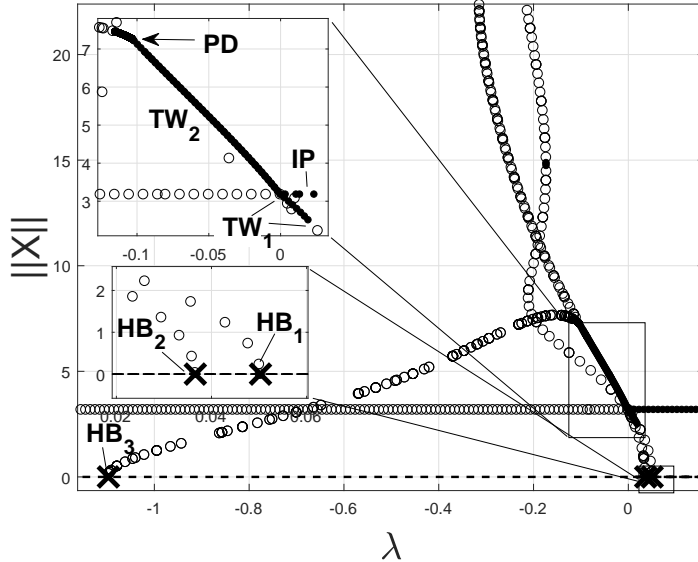


Figure 4.1. One-parameter bifurcation diagram as a function of λ for the ideal model with $N = 3$. Note that the stable orbit regions are qualitatively similar to those in the circuit model bifurcation diagram.

As a convention, dashed line represent unstable equilibrium points, empty circles represent unstable orbits, and filled-in circles represent stable orbits. Bold crosses denote Hopf bifurcation points. A single, unstable equilibrium was found at the trivial solution for all values of λ . Coinciding with the circuit model analysis, a branch of periodic solutions with group symmetry ($\mathbb{Z}_3, \mathbb{Z}_3$) runs parallel to the equilibrium whose existence is independent of λ . Three complex eigenvalue crossings of the imaginary axis corresponding to Hopf bifurcations were found at values $\lambda_{HB_1} = 0.0503$, $\lambda_{HB_2} = 0.0366$, $\lambda_{HB_3} = -1.097$. Note that the asymptotic approximations calculated for these values from Section 4.2 are relatively close with the exception of HB_3 . The eigenvalue approximation loses accuracy as we move far from the point of perturbation, $\lambda = 0$. All solutions emerging from these Hopf bifurcations display TW patterns with isotropy subgroup ($\mathbb{Z}_3, \mathbb{1}$). HB_1 and HB_3 are generated by $\gamma^2 = \langle \frac{2T}{3} \rangle$ and HB_2 is generated by $\gamma^1 = \langle \frac{T}{3} \rangle$. The reason that two distinct Hopf bifurcations and their respective solution branches lead to the same pattern and generator is seen in our two-parameter bifurcation diagram, Fig. 4.2. The Hopf path labeled as HB_1 crosses twice at the fixed parameter value $g = 1.1$. Thus, both HB_1 and HB_3 belong to the same Hopf locus and corresponding group symmetry. The TW_1 branch emerging from HB_1 shows stable periodic solutions for small positive λ values at approximately $0 < \lambda < 0.025$. Similar to the

findings from the circuit model analysis, this region is also populated by stable IP solutions. Stable limit cycles with TW_2 pattern were located for small negative λ values $-0.1 < \lambda < 0$. This is the only stable type of solution observed in this region. If we continue performing numerical continuation and decrease our value of λ past -0.1 , a small pocket of TW solutions that have gone through a period doubling bifurcation can be seen. These quickly lose stability as we move deeper into the negative regime. Referring back to our two-parameter bifurcation diagram, TW solutions exist exclusively in the regions above the two Hopf locus seen in Fig. 4.2. The locus for HB_2 does not continue past small g values. This is consistent with the bifurcation analysis performed in Section 2.5.

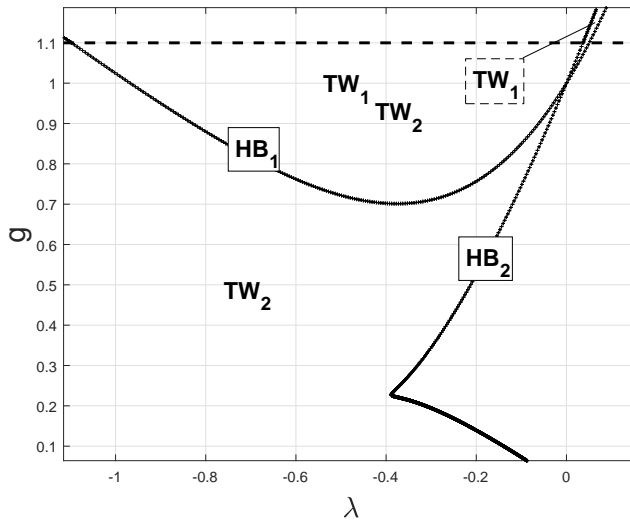


Figure 4.2. Two-parameter bifurcation diagram showing the Hopf bifurcation locus. Note that for large enough fixed values of g , the locus corresponding to HB_1 will cross the fixed g space twice.

We now proceed to analyze the case $N = 4$. Figure 4.3 shows the one-parameter bifurcation diagram with varying λ . A major difference between this diagram and that of $N = 3$ is that our equilibrium point is not invariant under changes in λ . The trivial equilibrium still populates our system but branches off into multiple equilibria for negative λ values between approximately $-1.6 < \lambda < 0$. However, the limit cycle branch with $(\mathbb{Z}_4, \mathbb{Z}_4)$ symmetry only runs parallel to the trivial solution. Three Hopf bifurcations were found at values $\lambda_{HB_1} = 0.08563$, $\lambda_{HB_2} = 0.04959$, and $\lambda_{HB_3} = -1.061$. Disregarding the change in equilibrium behavior, cases $N = 3$ and $N = 4$ share similar Hopf and solution behavior. HB_1 and HB_3 emerge from the same Hopf locus which can be seen in Fig. 4.4. Both Hopf bifurcations branch into solutions with the same TW pattern generated by $\gamma^3 = \langle \frac{3T}{4} \rangle$ with

group symmetry $(\mathbb{Z}_5, \mathbb{1})$. HB_2 solutions belong to the same isotropy subgroup but is generated by $\gamma^1 = \langle \frac{T}{4} \rangle$.

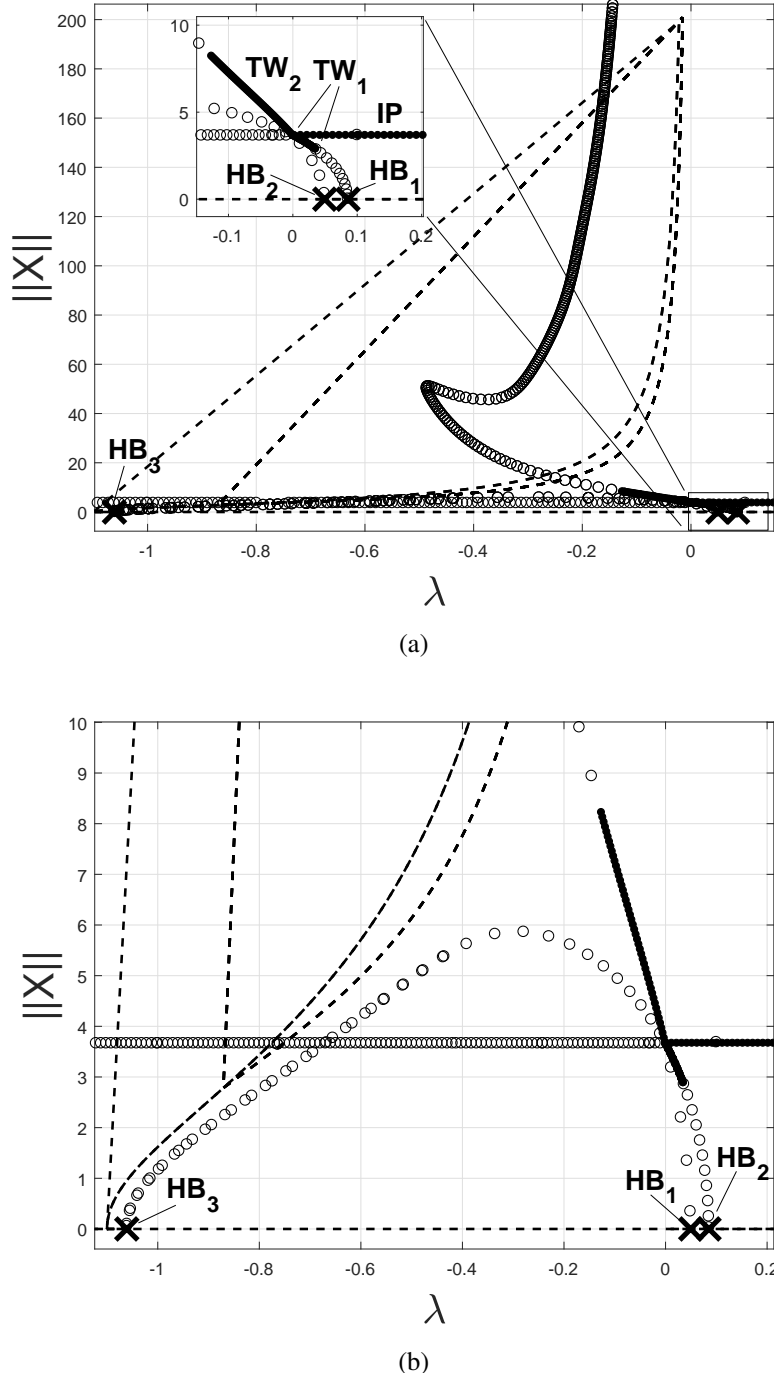


Figure 4.3. (a) One-parameter bifurcation diagram of varying λ for the ideal model representing the case of four coupled Colpitts Oscillators. **(b)** Close up to trivial solution and Hopf bifurcations.

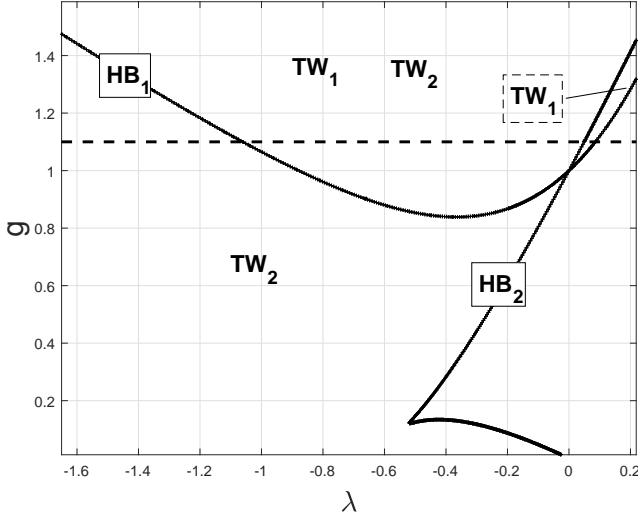


Figure 4.4. Two-parameter bifurcation diagram varying λ and R_L for the ideal model representing the case of four coupled oscillators.

Figure 4.5 shows the one-parameter bifurcation diagram for $N = 5$. Four different Hopf bifurcations were located at values $\lambda_{HB_1} = 0.1386$, $\lambda_{HB_2} = 0.06591$, $\lambda_{HB_3} = 0.03875$, $\lambda_{HB_4} = -1.013$, and $\lambda_{HB_5} = -1.104$. All Hopf bifurcations are part of the isotropy subgroup $(\mathbb{Z}_5, \mathbb{1})$. HB_1 and HB_4 share the same locus, see Fig. 4.6, and their respective solution pattern, TW_1 is generated by $\gamma^4 = \langle \frac{4T}{5} \rangle$. This case includes a second pair of Hopf bifurcations that share the same Hopf locus, HB_2 and HB_5 . They are both generated by $\gamma^1 = \langle \frac{T}{5} \rangle$, and we label the solution pattern as TW_2 . The TW patterns observed for the case $N = 5$ are as follows:

$$\begin{aligned} TW_1 &:= X(t) = \left(x_1(t), x_1 \left(t + \frac{4T}{5} \right), x_1 \left(t + \frac{3T}{5} \right), x_1 \left(t + \frac{2T}{5} \right), x_1 \left(t + \frac{T}{5} \right) \right); \\ TW_2 &:= X(t) = \left(x_1(t), x_1 \left(t + \frac{T}{5} \right), x_1 \left(t + \frac{2T}{5} \right), x_1 \left(t + \frac{3T}{5} \right), x_1 \left(t + \frac{4T}{5} \right) \right); \\ TW_3 &:= X(t) = \left(x_1(t), x_1 \left(t + \frac{3T}{5} \right), x_1 \left(t + \frac{T}{5} \right), x_1 \left(t + \frac{4T}{5} \right), x_1 \left(t + \frac{2T}{5} \right) \right). \end{aligned}$$

The case $N = 6$ displays similar symmetry to the three previously seen cases, with the exception of the emergence of the symmetry group $(\mathbb{Z}_6, \mathbb{Z}_2)$ as seen in Section 3.2. This pattern is generated by $\gamma^1 = \langle \frac{2T}{3} \rangle$ and appears from two symmetry breaking bifurcations, HB_3 and HB_7 , that belong to the same Hopf locus. This pattern is labeled as a variant of the SW, $SW_{2,1}$. The solution generated by $\gamma^2 = \langle \frac{T}{3} \rangle$ with the same group symmetry is a consequence of the symmetry breaking bifurcation, HB_4 . Hopf bifurcations were found at values $\lambda_{HB_1} = 0.2118$, $\lambda_{HB_2} = 0.08442$, $\lambda_{HB_3} = 0.05031$, $\lambda_{HB_4} = 0.0366$, $\lambda_{HB_5} = 0.03197$,

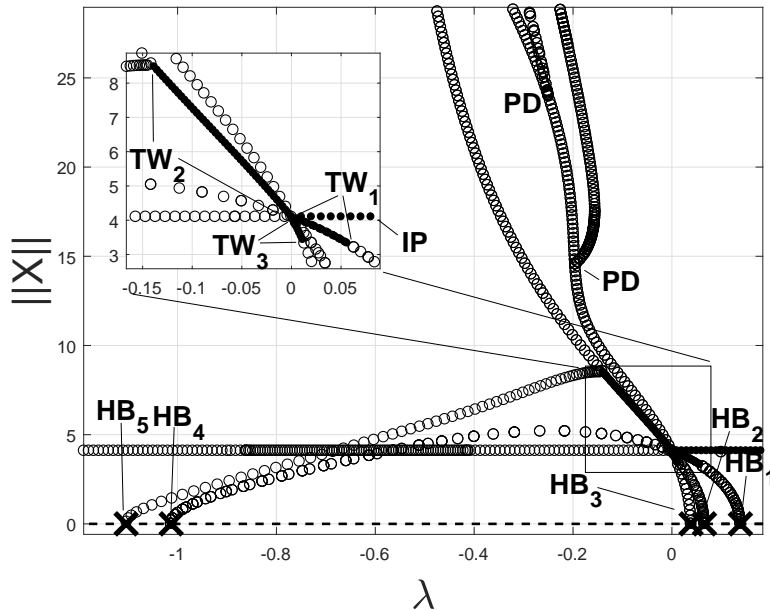


Figure 4.5. One-parameter bifurcation diagram of varying λ for the system describing the ideal model of five coupled Colpitts oscillators.

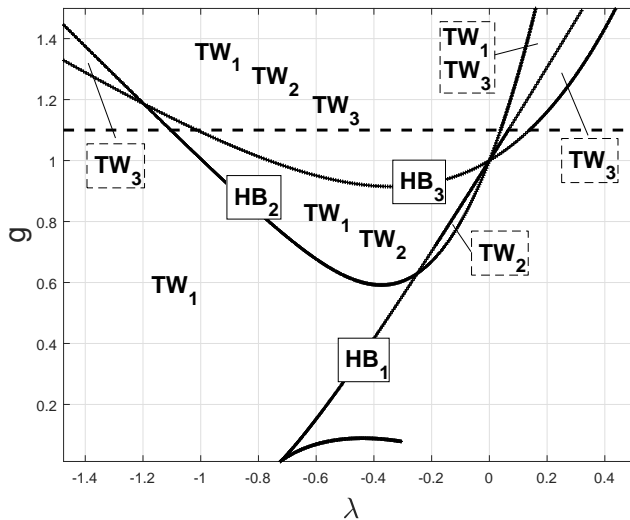


Figure 4.6. Two-parameter bifurcation diagram for the system describing the ideal model of five coupled Colpitts oscillators.

$\lambda_{HB_6} = -0.9654$, and $\lambda_{HB_7} = -1.097$. HB_1 and HB_6 both give rise to TW_1 solutions generated by $\gamma^5 = \langle \frac{5T}{6} \rangle$. The TW pattern generated by $\gamma^1 = \langle \frac{T}{6} \rangle$ appears after HB_2 which we label TW_2 . Lastly, the solution that belongs to pattern $(\mathbb{Z}_6, \mathbb{Z}_3)$, labeled SW_1 , is generated by $\gamma^3 = \langle \frac{T}{6} \rangle$ and produced from HB_5 . Fig. 4.8 shows that similar to previous cases, Hopf bifurcations do not exist for values of g that are too small. This is consistent with the analysis

done on a single Colpitts oscillator in Section 2.5. Note that as we increase the number of coupled oscillators, the high number of Hopf locus intersections makes partitioning the (λ, g) plane into solution regions difficult. The merit of all these bifurcation results becomes apparent in the next section where we discuss the experimental work done on NCCOs with intent of building a precision timing device.

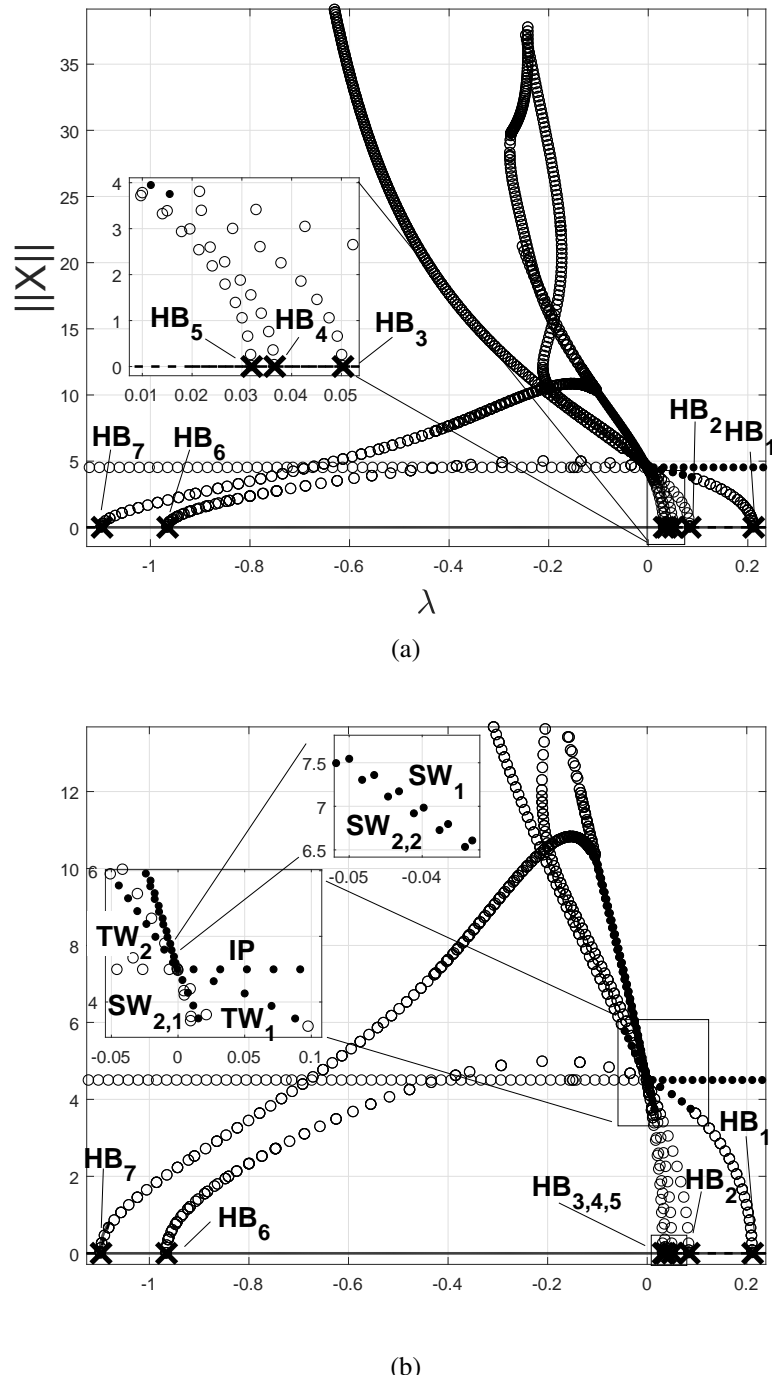


Figure 4.7. (a) One-parameter bifurcation diagram of varying λ for the ideal model of six coupled Colpitts oscillators. **(b)** Close up to trivial solution and Hopf bifurcations.

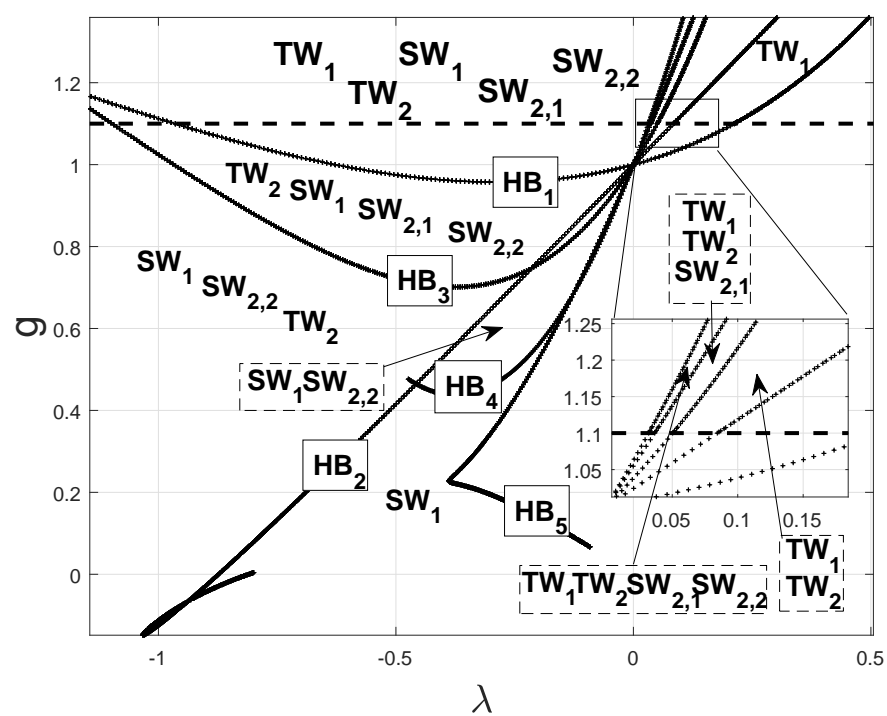


Figure 4.8. Two-parameter bifurcation diagram of the ideal model with six coupled Colpitts oscillators.

CHAPTER 5

EXPERIMENTS

The work outlined in this thesis will work as mathematical validation for observed collective behavior in NCCOs. Ensembles of unidirectionally coupled Colpitts oscillators for the purpose of precision timing have been built by research teams in NWIC Pacific and University of California, Los Angeles (UCLA). An image of a prototype built on a Printed Circuit Board (PCB) can be seen in Fig. 5.1. The circuit board allows for controlling the number of active coupled oscillators. Thus, different numbers of oscillators can be studying without the need of building separate circuit boards.

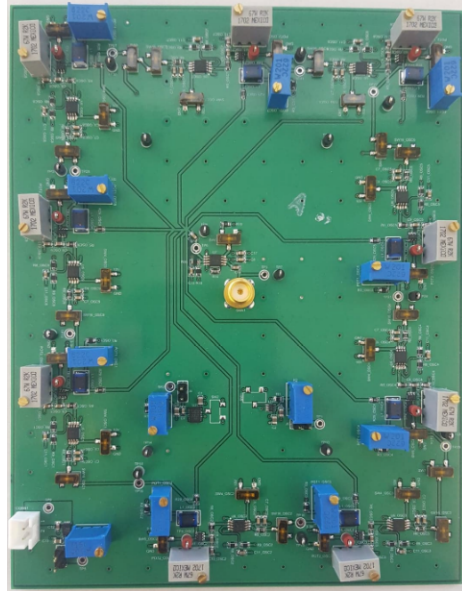


Figure 5.1. PCB prototype with nine unidirectionally coupled oscillators. It allows for controlling the number of active Colpitts oscillators.

Experiments have concentrated on observing the behavior and calculating phase drift error for odd number of coupled oscillators with TW configuration using the PCB in Fig. 5.1. Recall that the TW pattern was globally asymptotically stable only for small, negative coupling strength values. This negative coupling is introduced into the circuit by inverting the signal from one oscillator and applying it to the next oscillator. This is achieved by using an inverting operational amplifier. Measurements approaching the $1/N$ scaling have been observed by comparing the phase drift of coupled oscillators vs the phase drift of a single

Colpitts oscillator as seen in Fig. 5.2. In practice, the phase drift is calculated by measuring the power spectrum ratio of the signal at a 1 MHz offset from the carrier frequency. Figure 5.2 shows for cases $N = 5$ and $N = 7$, the network of coupled oscillators with TW configuration have a 4.47 and 6.23 times accuracy improvement when compared to a single, uncoupled Colpitts oscillator. When compared to the uncoupled ensemble, the coupled case is 2.00 and 2.35 times more accurate for the case $N = 5$ and $N = 7$ respectively. This shows great promise and provides hard evidence that coupling the network of Colpitts oscillators provides a significant improvement in the precision of the device. Measurements for the cases $N = 3$ and $N = 7$ were not recorded due to difficulties at the time of the experiment. However, the built network of oscillators is still being studied.

SCALING FACTOR * (with respect to single oscillator)				
N	UNCOPLED*	COUPLED*	Improvement COUPLED vs. UNCOUPLED	Summed Frequency (MHz)
3	1.73	NA	NA	3.12
5	2.24	4.47	2.00	5.002
7	2.65	6.23	2.35	7.151
9	3.00	NA	NA	NA

Figure 5.2. Measured phase drift improvement for ensembles of five and seven oscillators. The improvement approaches the desired $1/N$ scaling.

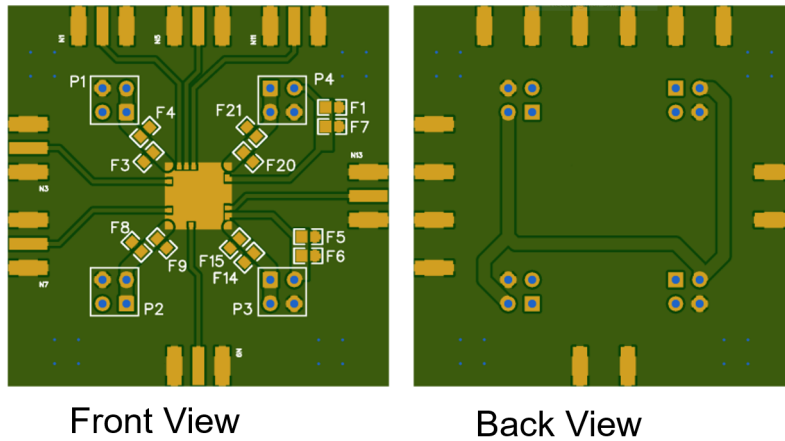


Figure 5.3. PCB design for voltage measurement of chip-scale NCCO.

A team in UCLA has been developing a chip-scale version of the system of Colpitts oscillators. The miniaturized Colpitts oscillator has been re-designed as an inductor-less circuit to avoid signal contamination due to the magnetic field created by inductors in close

proximity. The design of the PCB designed for chip measurement is seen in Fig. 5.3, and the summed output of a chip-scale ensemble of three Colpitts oscillators can be seen in Fig. 5.4. Similar setups as the one seen in Fig. 5.3 will allow for the fabrication of compact devices that contain a high number of chip-scale Colpitts oscillators. This will allow the device to reach ultra precision accuracy while remaining portable. The voltage reading seen in Fig. 5.4 consists of summing the voltage output of each individual chip-scale oscillator. Summing the voltage output is common in practice and allows for easier time measurements. However, phase drift calculations have not been made for the miniaturized ensemble. This is work still in progress by the research team in UCLA.

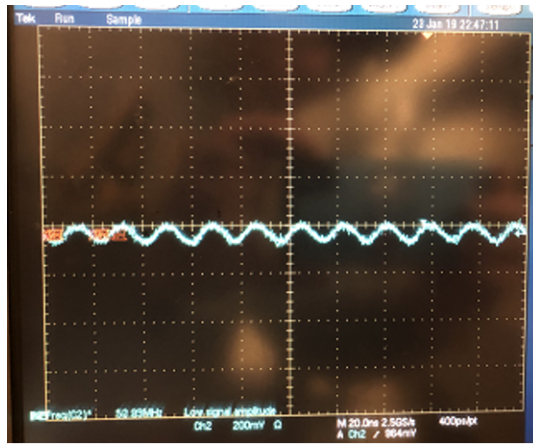


Figure 5.4. Measured sum output of three chip-scale col-pitts oscillators.

The work detailed in this thesis mathematically validates experimental results and improves the dependability of the precision timing device being built.

CHAPTER 6

DISCUSSION AND FUTURE WORK

Precision timing is crucial to modern civilization. Most of the world depends on GPS in order to obtain highly precise time measurements. However, GPS is not accessible from all types of terrains and conditions. We propose building an ultra precision timing device from a network of Colpitts oscillators (NCCOs) coupled unidirectionally to meet the need of a highly accurate, GPS independent precision timing device. The device relies on the concept of reducing phase drift error as much as possible by exploiting different collective behavior of the NCCOs. The desired collective behavior of the system is the traveling wave solution pattern which reduces the error scaling to $1/N$ from $1/\sqrt{N}$. This thesis outlines different nonlinear analysis techniques used to find this traveling behavior and validate the error scaling improvement.

The work outlined in this thesis analyzing the governing equations of NCCO helps bring insight into the dynamics of the system. As a consequence of the system's underlying $\Gamma = \mathbb{Z}_N \times S^1$ symmetry, the existence of the desired TW pattern is guaranteed, and the numerical bifurcation analysis confirms the existence of TW stable limit cycles. The implementation of the ideal model simplifies the analysis and allows for approximate analytical calculations of the system's eigenvalues. The isotropic decomposition seen in Section 4.2 leads to a block diagonalization of the systems linearized matrix which allows for direct stability analysis of each possible solution. However, an analytical solution of system's eigenvalues is still pending. Preliminary phase drift calculations are seen in Section 3.5 which validate the theoretical scaling improvement. All of these analytical and numerical results are consistent with the experimental work detailed in Chapter 5. These theoretical, numerical, and experimental results show great promise for the future of timing devices built with the concept of coupled nonlinear oscillators.

Future work includes calculating more precise phase drift scaling measurements. A more in depth analysis of the stochasticity added to the system is needed in order to study the convergence of the Euler-Maruyama scheme. This would help further validate the phase drift calculations seen in Section 3.5. Future work also includes a generalized solution for all eigenvalues of the system. This would analytically validate the results seen in our numerical bifurcation analysis in Sections 3.3 and 4.3. Both of these tasks will greatly increase the mathematical foundation upon which the device is being built.

BIBLIOGRAPHY

- [1] *Stochastic Systems*, Mathematics in Science and Engineering, Elsevier Science, 1983.
- [2] *NIST launches a new U.S. time standard: NIST-F2 atomic clock*, Apr 2014.
- [3] E. BRUTON, *History of Clocks and Watches*, Collectors Reference Series, Crescent Books, 1979.
- [4] P. BUONO, B. CHAN, J. FERREIRA, A. PALACIOS, S. REEVES, P. LONGHINI, AND V. IN, *Symmetry-breaking bifurcations and patterns of oscillations in rings of crystal oscillators*, SIAM Journal on Applied Dynamical Systems, 17 (2018), pp. 1310–1352.
- [5] P.-L. BUONO, V. IN, P. LONGHINI, L. OLENDER, A. PALACIOS, AND S. REEVES, *Phase drift on networks of coupled crystal oscillators for precision timing*, Phys. Rev. E, 98 (2018), p. 012203.
- [6] O. DE FEO AND G. MARIO MAGGIO, *Bifurcations in the Colpitts oscillator: From theory to practice*, International Journal of Bifurcation and Chaos, 13 (2003).
- [7] E. DOEDEL AND X. WANG, *Auto97: Software for continuation and bifurcation problems in ordinary differential equations*, 1997.
- [8] B. ERMENTROUT, *Simulating, analyzing, and animating dynamical systems: A guide to xppaut for researchers and students*, Applied Mechanics Reviews, 56 (2003).
- [9] O. FEO, G. MARIOMAGGIO, AND M. KENNEDY, *The Colpitts oscillator: Families of periodic solutions and their bifurcations*, International Journal of Bifurcation and Chaos, 10 (2012).
- [10] C. GARDINER, *Handbook of Stochastic Methods for Physics, Chemistry, and the Natural Sciences*, Springer complexity, Springer, 2004.
- [11] M. GOLUBITSKY, I. STEWART, AND D. SCHAEFFER, *Singularities and Groups in Bifurcation Theory*, no. v. 2 in Applied Mathematical Sciences, Springer New York, 2000.
- [12] R. HOYLE, *Pattern Formation: An Introduction to Methods*, Cambridge University Press, 2006.
- [13] M. KENNEDY, *Chaos in the Colpitts oscillator*, IEEE Transactions on Circuits and Systems I: Fundamental Theory and Applications, 41 (1994), pp. 771–774.
- [14] M. LAKSHMANAN AND S. RAJASEEKAR, *Nonlinear Dynamics: Integrability, Chaos and Patterns*, Advanced Texts in Physics, Springer Berlin Heidelberg, 2012.
- [15] H. LYONS, *Atomic clocks*, Scientific American, Inc., (1957).
- [16] W. A. MARRISON, *The evolution of the quartz crystal clock*, The Bell System Technical Journal, 27 (1948), pp. 510–588.

- [17] M. SAN MIGUEL AND R. TORAL, *Stochastic Effects in Physical Systems*, Springer Netherlands, Dordrecht, 2000, pp. 35–127.
- [18] A. SEDRA AND K. SMITH, *Microelectronic Circuits*, Oxford series in electrical and computer engineering, Oxford University Press, 1998.
- [19] S. STROGATZ, *Nonlinear Dynamics and Chaos: With Applications to Physics, Biology, Chemistry, and Engineering*, Studies in Nonlinearity, Avalon Publishing, 2014.
- [20] B. VAN DER POL, *A theory of the amplitude of free and forced triode vibrations*, Radio Review, (1920).